

Ice dynamics and structural evolution of Jutulstraumen, Dronning Maud Land, East Antarctica (1963 – 2022_[AI])

Anwasha Sharma¹, Chris R. Stokes¹ and Stewart S.R. Jamieson¹

¹Department of Geography, Durham University, Durham, DH1 3LE, UK

Correspondence: Anwasha Sharma (Anwasha.sharma@durham.ac.uk)

Abstract

Jutulstraumen is a major outlet glacier in East Antarctica that drains into the Fimbulisen, Dronning Maud Land. Here, we present the first long-term (~60 years) record of its behaviour using optical satellite imagery. Our analysis reveals that the ice front has been steadily advancing since its last major calving event in 1967, with a steady ice flow velocity of $\sim 720 \pm 66 \text{ m yr}^{-1}$ (2000-2021), accompanied by spatially variable thickening of the grounded ice at $+0.14 \pm 0.04 \text{ m yr}^{-1}$ (2003-2020). We also find evidence to suggest a minor grounding line advance of $\sim 200 \text{ m}$ between 1990 and 2022, albeit with large uncertainties. Mapping of the major rifts on Jutulstraumen’s ice tongue (2003-2022) reveals an overall increase in their length, accompanied by some minor calving events along its lateral margins. Given the present-day ice front advance rates ($\sim 740 \text{ m yr}^{-1}$), the ice tongue would reach its most recent maximum extent (attained in the mid-1960s), in around 40 years, but extrapolation of rift lengthening suggests that a major calving event may occur sooner, possibly in the late 2050s. Overall, there is no evidence of any dynamic imbalance, mirroring other major glaciers in Dronning Maud Land.

1. Introduction

The Antarctic Ice Sheet (AIS) is losing mass due to anthropogenic climate warming (Meredith and others, 2019; The IMBIE team, 2023). Recent satellite observations reveal that total mass loss from the AIS has accelerated in the past few decades (Rignot and others, 2013, 2019; Schröder and others, 2019), dominated by the West Antarctic Ice Sheet (WAIS) which has an average imbalance of $-82 \pm 9 \text{ Gt yr}^{-1}$ from 1972-2020 (The IMBIE Team, 2023). The ongoing response of the AIS to atmospheric and oceanic warming raises concerns about its future contribution to sea level rise (McGranahan and others, 2007; Oppenheimer and others, 2019). Furthermore, paleoclimate records (Noble and others, 2020) and ice sheet models (Nowicki and others, 2013; DeConto and Pollard 2016; Seroussi and others, 2020; Payne and others, 2021) highlight that the AIS was highly sensitive to periods of warming in the past (Fogwill and others, 2014-). These periods are often used as an analogue for mass loss with respect to future atmospheric warming projections (DeConto and others, 2021).

Whilst mass loss from the WAIS has been detected since the early 1990s (The IMBIE Team, 2023), the East Antarctic Ice Sheet (EAIS) is thought to have been broadly in balance or slightly positive, with a recent estimate of $+3 \pm 15 \text{ Gt yr}^{-1}$ between 1992 and 2020 (The IMBIE team, 2023). However, the EAIS has been responding to ocean-climate forcing in a spatially variable manner, with

This is an Open Access article, distributed under the terms of the Creative Commons Attribution licence (<http://creativecommons.org/licenses/by/4.0>), which permits unrestricted re- use, distribution and reproduction, provided the original article is properly cited.

notable mass gains in Dronning Maud Land (DML) and considerable mass loss from the Wilkes Land sector, in particular (Shepherd and others, 2012; Khazendar and others, 2013; Greenbaum and others, 2015; Li and others, 2016; Medley and others, 2018; Rignot and others, 2019; Brancato and others, 2020; - Smith and others, 2020; Stokes and others, 2022; The IMBIE team, 2023). The average mass balance of DML between 1992 and 2017, comprising basins 5 to 8 (Fig.1) as defined by Zwally and others (2012), has been estimated at $+13.3 \pm 3.4 \text{ Gt yr}^{-1}$ (Shepherd and others, 2020), with the Shirase Glacier catchment contributing to $+46 \text{ Gt}$ ($\sim 1.2 \text{ Gt yr}^{-1}$) of mass gain between 1979 and 2017 (Rignot and others, 2019). This mass gain in Shirase Glacier that began around 2000 (Schröder and others, 2019; Smith and others, 2020), has been attributed to a thickening of the floating ice tongue (Schröder and others, 2019; Smith and others, 2020) and the subsequent deceleration of ice flow upstream of the grounding line (Miles and others, 2023). This process has been influenced by strengthening of alongshore winds, which limit the inflow of warm modified Circumpolar Deep Water (mCDW) into the Lützow-Holm Bay (Miles and others, 2023). In contrast, Wilkes Land (basin 13 in Fig. 1) exhibited a negative mass balance, estimated at $-8.2 \pm 2.0 \text{ Gt yr}^{-1}$ between 1992 and 2017 (Shepherd and others, 2019) with Totten Glacier losing -236 Gt ($\sim -6.2 \text{ Gt yr}^{-1}$) of ice between 1979 and 2017 (Rignot and others, 2019). This mass loss in Wilkes Land has been associated with intrusion of warm mCDW into the deep troughs connecting the glacier cavity to the ocean and resulting in enhanced basal melt (Miles and others, 2016; Rignot et al. 2019). Thus, the EAIS response to climate change is complex and varies from basin to basin (cf. Stokes and others, 2022).

Although DML has been gaining mass over recent decades, some studies indicate an increase in basal melt due to Warm Deep Water (WDW) influx (Lauber and others, 2023) and predict significant mass loss under future warming scenarios (Golledge and others, 2015, 2017; DeConto and others, 2021). Observations at Fimbulisen between December 2009 and January 2019 indicate an increase in the influx of Warm Deep Water (WDW) after 2016, resulting in an increase in basal melt rate of $\sim 0.62 \text{ m yr}^{-1}$ (Lauber and others, 2023). This change has been linked to decline in sea ice concentrations and intensified subpolar westerlies in the region (Lauber and others, 2023). Furthermore, model predictions have suggested that the Recovery Basin in DML will be vulnerable to increasing ocean temperatures under a high emissions future warming scenario (Golledge and others, 2015, 2017). Indeed, some studies suggest substantial mass loss in the DML region by 2300 following a 3°C warming emission scenario (DeConto and others, 2021), albeit with high uncertainties. As such, continued increases in incursion of warm water events and projected future warming could further increase basal melt, thereby impacting the ice shelf mass balance in DML earlier than anticipated. However, there exists a gap in systematic observations of glacier dynamics of major glaciers in this region. Without those observations it is challenging to understand the ongoing regional response to current and future climate change.

Our aim is to conduct the first long-term, systematic observations of Jutulstraumen, one of the largest outlet glaciers in DML, to improve our understanding of its recent dynamics from the 1960s to present (2022) and explore its future dynamics. This is undertaken using remotely sensed satellite imagery and several secondary datasets to analyse changes in glacier dynamics based on: (1) ice

front positions; (2) ice velocity (Gardner and others, 2019; ENVEO, 2021); (3) surface elevation change (Schröder and others, 2019; Smith and others, 2020; Nilsson and others, 2022); (4) grounding line position (Harran and others, 2005, 2014; Bindschadler and others, 2011; Rignot and others, 2016) and (5) structural mapping (Fricker and others, 2005; Holt and others 2013; Walker and others, 2015).

2. Study area and previous work on Jutulstraumen

The Fimbulisen (FIS) is the largest ice shelf in the EAIS ($\sim 39,400 \text{ km}^2$) located between 71.5°S to 69.5°S and 3°W to 7.5°E . Jutulstraumen ('The Giant's Stream' in Norwegian) is a fast-flowing ice stream ($\sim 700 \text{ m yr}^{-1}$) that feeds the central part of the ice shelf (Figs.1, 2, Lunde, 1963; van Autenboer & Declair, 1969; Gjessing, 1970) and has an annual ice discharge of $30 \pm 2.2 \text{ Gt yr}^{-1}$ between 2009 and 2017 (Rignot and others, 2019). The average mass balance of Jutulstraumen has been estimated at $+33 \text{ Gt}$ between 1979 and 2018 (Rignot and others, 2019). There has been only one major calving event recorded between the 1960s and 2022, occurring in 1967 (van Autenboer & Declair, 1969; Vinje, 1975; Swithinbank and others, 1977; Kim and others, 2001) when a $\sim 100 \text{ km}$ long by $\sim 50 \text{ km}$ wide iceberg calved from Jutulstraumen's floating ice tongue (named 'Trolltunga') along newly formed perpendicular rifts (Vinje 1975; Humbert & Steinhage, 2011). This calved iceberg then drifted along the Weddell Sea for more than 13 years (Vinje, 1975).

Jutulstraumen is pinned by ice rises on either side of the ice tongue (Kupol Moskovskij to the east and Bløskimen and Apollo Island to the west) (Matsuoka and others, 2015; Figs. 1,2), which may influence the flow and contribute to a stabilising effect on the current ice shelf configuration (Melvold & Rolstad, 2000; Goel and others, 2020). The main trunk of Jutulstraumen drains a major valley that ranges between 20-200 km wide and begins $\sim 60 \text{ km}$ inland of the modern grounding line and cuts through a significant coastal mountain range: the massifs Sverdrupfjella to the east and Ahlmannryggen to the west (Fig. 2, Humbert & Steinhage, 2011). The valley through which Jutulstraumen flows is a graben resulting from major rifting following the breakup of Gondwana (Fig. 1c, Declair & van Autenboer, 1982; Wolmarans and Kent 1982; Melvold & Rolstad, 2000; Ferraccioli and others, 2005). The depth of the Jutulstraumen trough, estimated at $\sim 1500 \text{ m}$ below sea level at the deepest part (Fig. 1, Gjessing, 1970; Declair & Autenboer, 1982; Melvold & Rolstad, 2000), allows the ice to drain from the EAIS interior and has the potential to make the area susceptible to ocean warming. However, recent modelling has explored the sensitivity of Jutulstraumen to mid-Pliocene warming (Mas e Braga and others, 2023), a period which is often used as an analogue for a near-future climate state (DeConto and others, 2021), and their findings highlight that the ice stream thickens by around 700 m , despite its retrograde bed slope. This thickening was attributed to lateral stresses at the flux gate constricting ice drainage and thus stabilising the grounding line (Mas e Braga and others, 2023).

Previous research suggests that recent (2010-2011) ocean conditions were relatively cold and dominated by Eastern Shelf Water in the cavity beneath the ice tongue (Hattermann and others, 2012), with an estimated mean basal melt rate of $\sim 1 \text{ m yr}^{-1}$ based on interferometric radar and GPS-derived strain rates in the central part of Fimbulisen (Langley and others, 2014). The basal melt rate

has been shown to vary between 0.4 and 2.8 m yr⁻¹ based on the different methods used, such as oceanographic measurements (Nicholls and others, 2008; Hattermann and others, 2012), satellite altimetry and InSAR data (Shepherd and others, 2010; Pritchard and others, 2012; Depoorter and others, 2013; Rignot and others, 2013), and oceanographic modelling (Smedsrud and others, 2006; Timmermann and others, 2012). However, recent observations show pulses of Warm Deep Water (WDW) entering the cavity since around 2016, occasionally reaching over -1.5 °C, with peak temperatures up to 0.2 °C, contributed to a basal melt rate of 0.62 m yr⁻¹ and which has been linked to mass loss of 15.5 Gt yr⁻¹ between 2016 and 2019 (Lauber et al., 2023). These changes, driven by a positive Southern Annular Mode (SAM) resulting in stronger westerlies and reduced sea ice, could significantly impact the ice shelf's mass balance and its buttressing effect on inland ice.

In summary, the response of EAIS to climate change is complex and varies across different regions. This is influenced by factors such as presence or absence of warm ocean conditions and bed topography (Morlighem and others, 2020). The lack of observational data for several major outlet glaciers, including Jutulstraumen, makes it even more challenging to understand how the glaciers in the EAIS are currently responding, or will respond to, changing climate. Thus, in this paper, we conduct systematic observations of Jutulstraumen between the 1960s and 2022 with the aim of improving our understanding of the changing ice conditions in this part of DML.

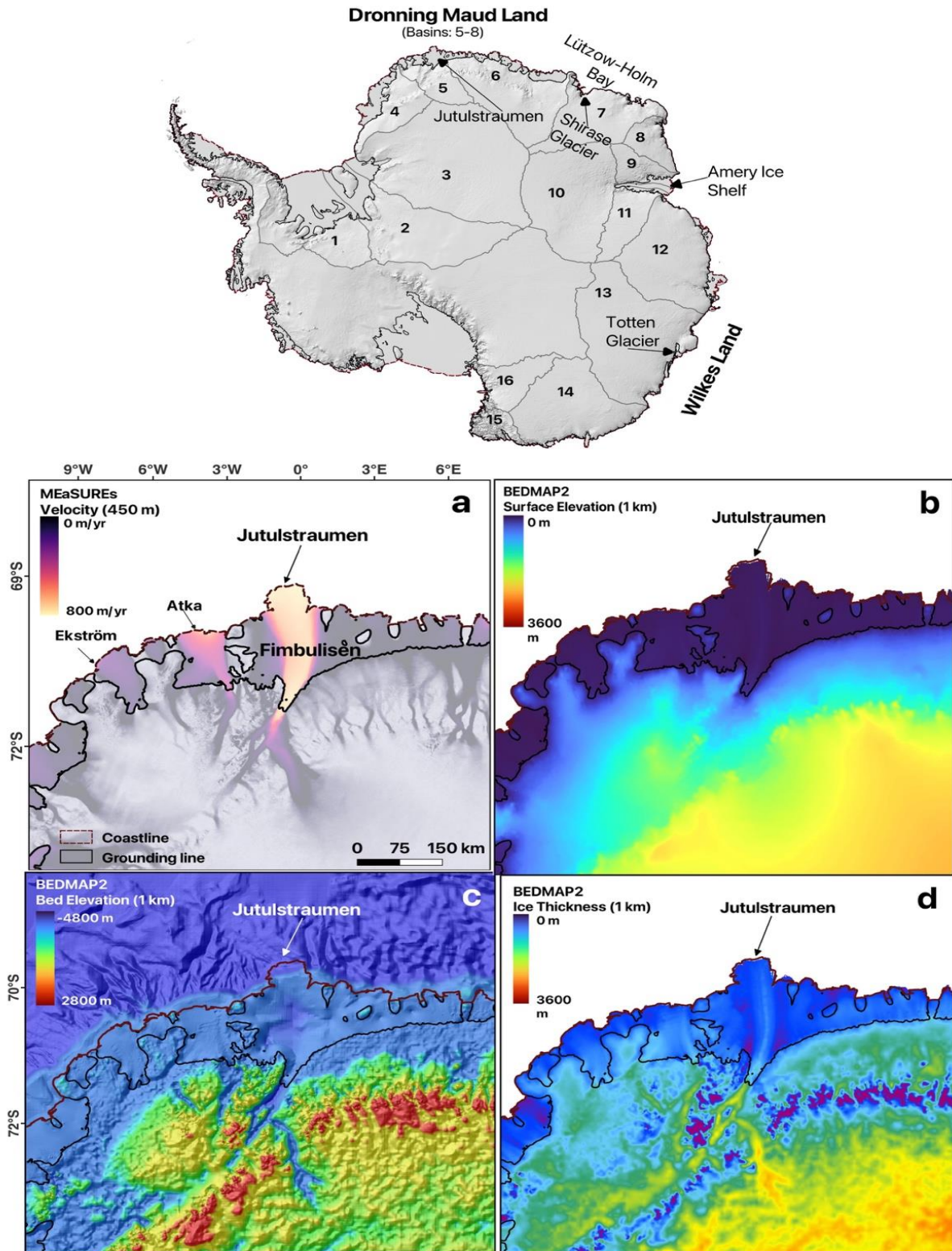


Fig. 1: Regional glacial and topographic setting of Jutulstraumen in DML, with numbers referring to drainage basins in the EAIS. (a) MEaSUREs (Rignot and others, 2016) ice flow speed of the study area, (b) Surface elevation of the study area using Bedmap2, (c) Bed elevation of the study area using Bedmap2, (d) Ice thickness of the study area using Bedmap2. Bedmap2 is sourced from Fretwell and others (2013). The grounding line and coastline are from Rignot and others (2017). Note that grid spacing in panel 'a' is 400 m and in panels 'b-d' is 1 km.

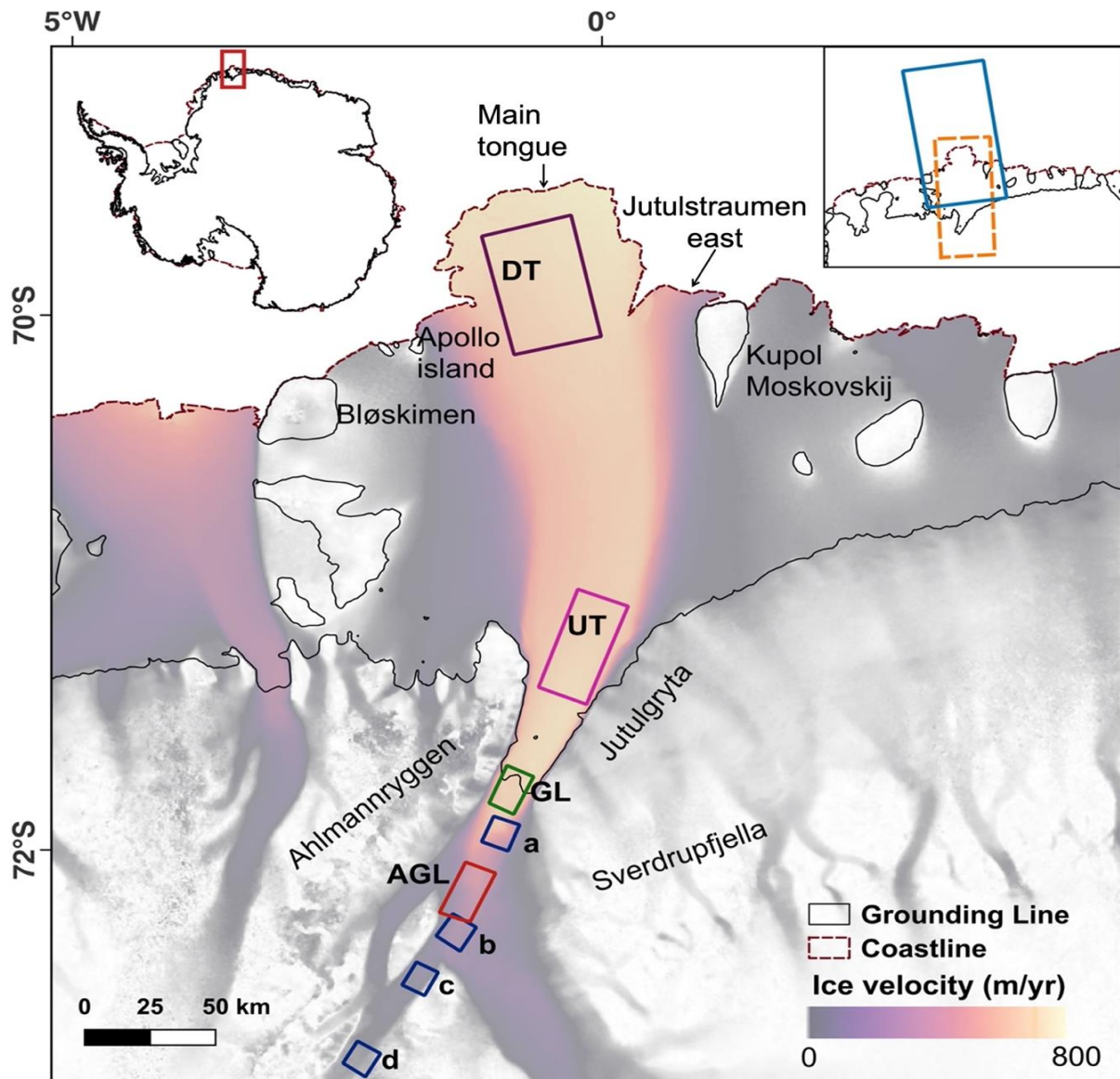


Fig. 2: Location map of Jutulstraumen, EAIS overlain with MEaSURES ice velocity. Grounding line (solid black) and coastline (dashed maroon) is from MEaSURES (Rignot and others, 2017). Velocity analysis is undertaken in each of the four boxes in the map marked as down-ice tongue (DT), up-ice tongue (UT), grounding line (GL) and above grounding line (AGL). Location of 20 x 20 km sampling boxes (navy blue) used to extract elevation change data from Schröder and others (2019), Smith and others (2020) and Nilsson and others (2022). Each sample box represents a specific distance from the grounding line to understand the surface elevation change at (a) 20 km, (b) 60 km, (c) 80 km and (d) 120 km from the grounding line. Note that the sample boxes used for elevation change are different from those used for ice velocity measurements because the velocity analyses primarily focus on changes at and downstream of the grounding line, whereas the elevation change were designed to capture major changes extending further upstream into the catchment area. ERA-5 2 m air temperature data were extracted from the dashed orange box and Nimbus-7 sea ice concentration data were extracted from the solid light blue box (top right insert).

3. Data and Methods

3.1. Ice front position change

In this study, a combination of satellite images from Landsat 1 MSS (1973-1974), Landsat TM 4 and 5 (1989-91), Landsat 7 ETM+ (1999-2013) and Landsat 8 OLI/TIRS (2013-2022) with cloud-free conditions were acquired from the USGS Earth Explorer website (<https://earthexplorer.usgs.gov>) to map changes in Jutulstraumen between 1963 and 2022 (Table S1). In addition, we use an orthorectified declassified ARGON satellite photograph of 1963 (Kim and others, 2001). A time series of ice front position change was generated between 1963 and 2022 based on the availability of imagery during the austral summer in the broadest sense (October-April). The annual ice front positions were manually digitised using ArcGIS Pro 2.8.2. The changes in position were quantified using the well-established box method which accounts for any uneven changes along the ice front (Moon & Joughin, 2008). Given the shape and orientation of Jutulstraumen's main ice tongue (Fig. 4), a curvilinear box was used (Lea and others, 2014). It should be noted that, in addition to the main outlet of Jutulstraumen, there exists an ice front along the eastern margin, separated by a rift, referred to as Jutulstraumen east hereafter (Figs. 2, 4c-d). The curvilinear box method was applied separately here. The errors in our measurements arise from co-registration of the satellite images (Landsat 1-8) with a 2022 Landsat-8 base image (which is quantified as the offset between stable features in image pairs, generally estimated at 1 pixel) and the manual digitisation of the ice front estimated at 0.5 pixels (Miles and others, 2013, 2016, 2018, 2021; Black and Joughin, 2022). The error was quantified using error propagation, considering the varying spatial resolutions of the imagery and the temporal gaps between them. The estimated error ranges from $\pm 3 \text{ m yr}^{-1}$ to $\pm 63 \text{ m yr}^{-1}$ (Table S1).

3.2. Glacier velocity

Average annual velocities were acquired from the Inter-mission Time Series of Land Ice Velocity and Elevation (ITS_LIVE) annual velocity mosaics (Gardner and others, 2018, 2019) between 2000 and 2018. These velocity mosaics were derived from a combination of Landsat -4, -5, -7 and -8 with the use of auto-RIFT feature tracking with each velocity mosaic having a spatial resolution of 240 m (Gardner and others, 2019). In addition, ENVEO (ENVEO and others, 2021) velocity mosaics were also used to extract velocity between 2019 and 2021. The ENVEO velocity mosaics were derived from repeat-pass Sentinel-1 Synthetic Aperture Radar (SAR) datasets using feature-tracking and are provided monthly between 2019 and 2021 at spatial resolution of 200 m. The monthly ENVEO velocity mosaics were averaged over 12-months for each year between 2019 and 2021 to compare with the ITS_LIVE annual velocity mosaics.

Velocities were extracted from the four regions shown in Fig. 2. Following Miles and others (2018) and Picton and others (2023), we calculated the mean annual velocities by averaging all available data within each sampling box, provided that data coverage of more than 20% was observed. However, a scarcity of data resulted in limited coverage, especially prior to 2000 (Table S2). Error estimates were provided for both datasets (Gardner et al., 2018, 2019; ENVEO et al., 2021), with each pixel having its own error term. The annual error values were then calculated by applying the

error propagation formula to the individual error values (grid cells) within each sample box for each ITS_LIVE annual velocity error mosaics (Gardner et al., 2018, 2019). Similarly, using error propagation, the monthly errors were calculated for the ENVEO velocity error mosaics. Subsequently, the annual velocity errors for 2019 to 2021 were computed using error propagation, accounting for the uncertainties in the monthly errors (ENVEO et al., 2021). Some of the velocity measurements were omitted from the analysis given the mean error from each sample box was more than 50% of the mean velocity magnitude (Miles and others, 2018; Picton and others, 2023) (Table S2). The accompanying errors associated with the velocity mosaics at DT, UT, GL and AGL ranged from ± 0.5 to $\pm 163 \text{ m yr}^{-1}$.

3.3. Elevation change

A range of previously published elevation change datasets were compared to understand any changes along Jutulstraumen. The elevation change measurements were extracted at four locations at 20 km, 60 km, 80 km and 120 km inland of the grounding line (Fig. 2). The average monthly elevation change was calculated by averaging all available data within each 20 x 20 km sample boxes (Fig. 2) using datasets provided by Schröder and others, (2019), Smith and others, (2020) and Nilsson and others, (2022). We use the accompanying uncertainty estimates provided with the three datasets and calculated the monthly error by applying the error propagation formula to the individual error values (grid cells) within each sample box.

The dataset provided by Schröder and others (2019) is a combination of multiple satellite missions (e.g., ERS-1/2, Geosat, Seasat, Envisat, ICESat and CryoSat-2) between 1978 and 2017, but referenced to September 2010. The dataset is provided with a horizontal resolution of 10 km and the associated monthly uncertainties at the sampling boxes range from ± 0.1 to $\pm 10 \text{ m yr}^{-1}$ (Schröder and others, 2019).

Nilsson and others (2022) provided a monthly elevation change dataset that spans from 1985 to 2020, with reference to December 2013. This dataset was produced as a part of the NASA MEaSUREs ITS_LIVE project. It also combines measurements from several satellite missions (e.g., ERS-1/2, Geosat, Seasat, Envisat, CryoSat-2, ICESat and ICESat-2) at a horizontal resolution of 1920 m. Monthly mean surface elevation change (SEC) was extracted from the same sampling boxes. The accompanying monthly uncertainties at the sample locations range from ± 0.05 to $\pm 3 \text{ m yr}^{-1}$. To allow a more direct comparison between the datasets, the SEC measurements from Schröder and others (2019) were recalculated relative to December 2013, aligning with the reference year used in Nilsson and others (2022). The two datasets were analysed from April 1992, as it is the earliest common data availability month at all four sample locations. We then calculate the 5-year moving averages for the two datasets. The errors associated with the 5-year moving average were determined from monthly errors using error propagation.

Additionally, the dataset provided by Smith and others (2020) is derived from ICESat and ICESat-2 missions, spanning from 2003 to 2019, with horizontal resolution of 5 km (Smith and others, 2020). The associated uncertainties range between ± 0.001 to $\pm 0.006 \text{ m yr}^{-1}$. To compare the three datasets, the mean rates of elevation change in each box were calculated for Schröder and others (2019) from

2003-2017, Smith and others (2020) from 2003-2019 and Nilsson and others (2022) from 2003-2020 (Table S3).

3.4. Grounding line changes

We analyse five previously published grounding line datasets spanning various dates between 1992 and 2018, along with new grounding line positions mapped in this study using manual digitisation between 1990 and 2022 (Fricker and others, 2009; Christie and others, 2016). Together, all these datasets were derived through either manual delineation or Differential Interferometric Synthetic Aperture Radar (DInSAR) techniques. It should be noted that each dataset identifies distinct features within the grounding zone, which makes comparison of changes through time more challenging (Fig. 7a, Fricker and others, 2009; Brunt and others, 2010). For example, the MEaSUREs grounding line dataset (Rignot and others, 2016) detects the landward limit of tidal flexure (F), ASAID dataset (Bindschadler and others, 2011) detects the break-in slope, I_b , whereas this study detects the local elevation minimum, I_m .

In this study, we manually delineate the grounding line positions using Landsat 4-8 images, during austral summers (October to April) between 1990 and 2022, following the methods outlined in Fricker and others (2009) and Christie and others (2016). As optical satellite imagery cannot precisely determine the “true” grounding line (G), the break-in-slope (I_b) or the local elevation minimum (I_m) (Fig. 7a) are generally used as a proxy for G . Here, we identify I_m as a shadow-like change in the brightness of the imagery (Fricker and Padman, 2006; Fricker and others, 2009; Bindschadler and others, 2011; Christie and others, 2016, 2018) and digitised it on the georeferenced cloud-free Landsat images. To determine whether the mapped grounding line advanced or retreated, we used the box method (Moon & Joughin, 2008), with the box extending to the ends of the mapped grounding lines. We used this method because it provides an average grounding line position change across the glacier. We also estimated a positional uncertainty of around ± 100 m, following Bindschadler and others (2011) and Christie and others (2016).

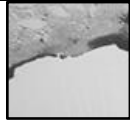
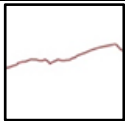
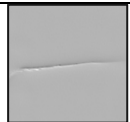
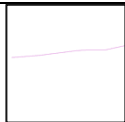
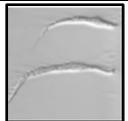
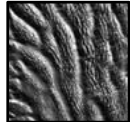
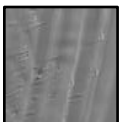
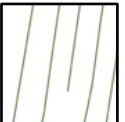
In addition, among the manually delineated grounding line datasets is the Antarctic Surface Accumulation and Ice Discharge (ASAID) dataset, which was created using a combination of photogrammetry applied to satellite imagery (primarily Landsat 7 ETM+), elevation profiles from ICESat data and visual analysis of optical satellite imagery. The grounding line was digitised on Landsat 7 ETM+ images between 1999 and 2003 by identifying changes in image brightness indicative of the break-in-slope (I_b). The average estimated positional uncertainty associated with the ASAID grounding line position for outlet glaciers is ± 502 m (Bindschadler and others, 2011). Similarly, The Mosaic of Antarctica (MOA) grounding line dataset was derived by manually delineating the most seaward break-in slope (I_b) on highly contrast-enhanced MOA surface morphology images (Scambos and others, 2007) for 2004 and 2009, with an associated uncertainty of ± 250 m (Harran and others, 2005, 2014). Furthermore, some grounding line positions are also derived using Differential Interferometric Synthetic Aperture Radar (DInSAR). The Making Earth Science Data Records for Use in Research Environments (MEaSUREs) dataset provides grounding line positions between 1992 and 2014, identifying the landward limit of tidal flexure (F). This dataset was derived using DInSAR from

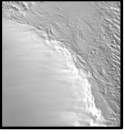
Earth Remote Sensing Satellites 1 and 2 (ERS-1 and ERS-2), RADARSAT-1, RADARSAT-2, the Advanced Land Observing System Phased Array type L-band Synthetic Aperture Radar (ALOS PALSAR), Cosmo Skymed, and Copernicus Sentinel-1 (Rignot and others, 2016). The associated uncertainty with the dataset is estimated at ± 100 m (Rignot and others, 2016). The European Space Agency's Antarctic Ice Sheet Climate Change Initiative (AIS CCI) has also been derived using DInSAR from ERS-1, ERS-2 and Sentinel-1 imagery collected between 1996 and 2020, with an estimated error of ± 200 m. In this dataset, the upper limit of vertical tidal motion has been used as an approximation of flexure point (F) in the grounding zone. The Mohajerani and others (2021) dataset employs a fully convolutional neural network to automatically delineate grounding lines for 2018 by identifying the landward limit of tidal flexure (F) using DInSAR data, with associated uncertainty of ± 232 m.

3.5. Structural glaciological mapping

To understand the structural glaciology of Jutulstraumen, some of the major surface structural features were manually mapped on selected cloud-free optical satellite imagery in 1986, 2001, 2015 and 2022 using bands with highest spatial resolution, e.g. band 4 in Landsat 1-4 and band 8 for Landsat 7 ETM+ and Landsat 8 OLI/TIRS (Holt and others, 2013; Table S1). The major structural features included rifts, fractures, crevasses, longitudinal flow features (flowstripes, flow bands, streaklines), surface expressions of major basal channels, ice rises and ice rumples. The criteria used to identify these various features is same as the approach taken by Glasser and others (2009) and Holt and others (2013) (Table 2), except for the identification of basal channels which has been adapted from Alley and others (2016).

Table 1: Ice-shelf features, examples, identifying criteria and significance adapted from (Glasser & Scambos, 2008; Glasser and others, 2009; Humbert & Steinhage, 2011; Holt and others, 2013)

FEATURE	EXAMPLE	STRUCTURE	IDENTIFICATION	SIGNIFICANCE
Ice front			Sharp transition from ice shelf margin to open ocean or sea ice. Sea ice is often seen as a darker shade than glacial ice in optical satellite imagery.	Indicates the maximum ice-shelf extent for particular time period. Successive images can be used to track fluctuation of ice front to understand ice dynamics.
Fracture			Appears as narrow, linear cracks visible as a sharp line	Indicative of stress within ice shelf.
Rift			Fractures on the ice shelf with visible opening, often form perpendicular to the ice-flow direction. The rifts could be filled with ice mélange, sea water or sea ice and penetrates the entire thickness of the ice shelf.	Rifts are indicative of integrity of an ice shelf. Rift tracking is a well-known method to estimate ice-flow velocity.
Crevasse field			Network of surface fractures that appear as dark (open or water filled) or bright (snow covered) linear lines. Crevasse often form in distinct zones (crevasse field).	Formed under conditions of sustained, widespread tensile stress within the ice and distributed across a larger zone, resulting in a region of organised fractures that develop perpendicular to maximum tension.
Fracture traces			Appears as narrow features or surface troughs similar to rift or fracture but without a clear opening or could be snow-filled.	Represents structural weaknesses in ice shelf and influences the mass and energy exchange between ice shelf and ocean (Luckman and others, 2012). They could also represent the surface expressions of basal crevasse (Luckman and others, 2012; McGrath and others, 2012).
Longitudinal surface structures			Long and linear pervasive surface feature parallel to the direction of ice-flow. These features are often tens or hundreds of km in length. They appear as dark and light lines due to shaded relief resulting from variation in brightness on slopes facing toward or away from solar illumination.	Typically indicates regions of faster ice flow and suture zones of different flow units (Glasser and Gudmundsson, 2012).

Surface expression of basal channels			These features appear as surface depressions starting at the GL, displaying abrupt shifts in their path. They usually align with the ice-flow direction and gradually dissipates towards ice-edge. These features appear to deepen or widen on the ice shelf (Alley and others, 2016).	Indicates basal melt and erosion of ice-shelf base. This might lead to development of crevasse zones and potentially weaken the ice shelf (Alley and others, 2016).
Ice rises			Elevation of the surface of ice shelf that disturbs the ice flow, indicated by smooth surface.	Indicates area of ice shelf grounded by local bedrock.
Mélange zone			Region that appears as filled with icebergs and sea ice, appears to have varying ice textures and wider than rift (Humbert & Steinhage, 2011).	It represents a typical shear margin.
Grounding zone			Sudden break-in slope and presence of intense crevasses. Sometimes melt water ponds tend to form at the grounding zone.	Intersection between grounded ice and floating ice (Vaughan, 1995).

To measure in more detail the rifts that propagate from the ice front into the ice tongue in more detail (Fig. 3), a total of 200 cloud-free images were selected. These images were collected during the austral summers between 2003 and 2022. They were obtained from the Moderate Resolution Imaging Spectroradiometer (MODIS) and have a spatial resolution of 250 m. For the purposes of this study, the austral summer is considered between October to early April (cf. Walker and others, 2015). Following the methodology in Fricker and others (2005), we measured the rift length from a consistent point at the ocean-end of the rift to the 'rift tip' (Fig. 3). The 'rift tip' was identified as the first point on the glacier where the rift pixel is discernible, i.e., the point in the image where rift occupied enough of the pixel to provide a good contrast against the background (Fricker and others, 2005; Walker and others, 2015; Holt & Glasser, 2022). Since these rifts are located at the ice front, it is possible that the ocean-end of the rifts may undergo discrete minor calving events between subsequent images, potentially leading to rift shortening. In such cases, when calving leads to rift shortening, the rift is assigned a new name to reflect the updated starting point. For example, RW3 becomes RW6, after the calving event in 2011 (Fig. 9a). This results in a consistent start point for the rifts across all subsequent images, enabling accurate measurement of rift propagation into the ice tongue. In addition, we determined the average annual and austral summer propagation rates by applying a linear fit to the time series data of rift lengths utilising the least squares method, following methodology outlined in Walker and others (2015). The linear regression analysis was performed to estimate slopes for each summer season for each rift (Case A, Table S4, S5). Case B represents the linear fit applied to the differences in rift lengths between the end of one summer and the start of the next summer. Case C denotes a linear fit applied to the entire dataset of rift lengths for each rift (Table S4, S5).

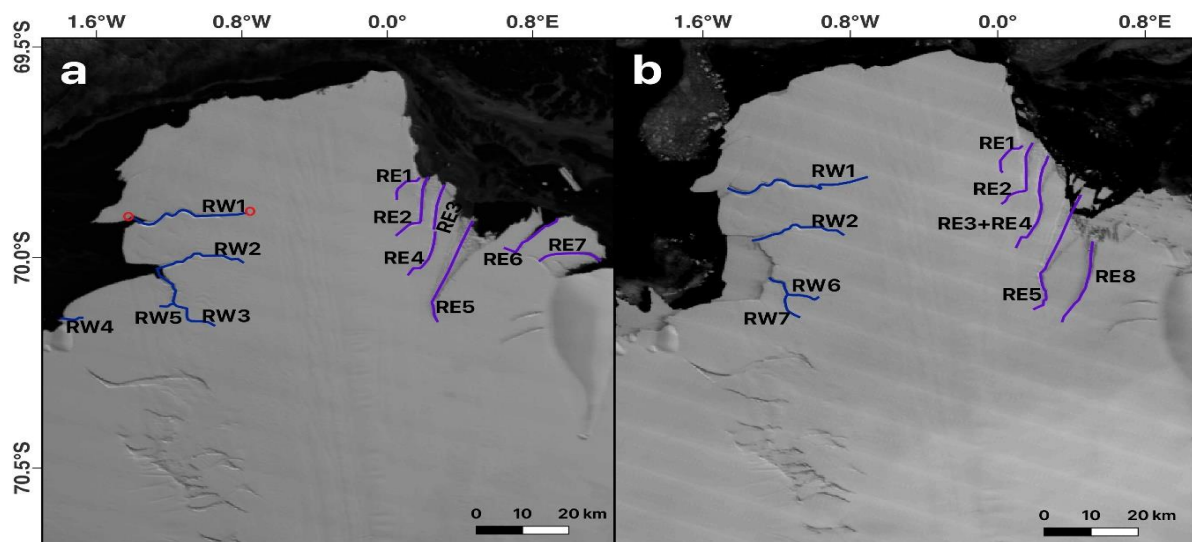


Fig. 3: (a-b) Rifting of the ice-shelf front monitored in this study (blue lines:western rifts (RW) and purple lines:eastern rifts (RE)) with background image: (a) MODIS images acquired on 13 March 2006 and (b) acquired on 16 December 2016. (b) shows the rifts formed later in the study period (RW6, RW7, RE8). It also shows that rift RE3 lengthened and joined RE4 (later named RE3+RE4). Note: Red circles in (a) denote start and end points for RW1, a front-initiated rift.

3.6. Relationship between rift propagation and environmental variables

To determine whether a relationship between rift propagation and environmental variables exists in Jutulstraumen (Basis and others, 2008; Walker and others, 2013; Walker and others, 2015), we compare the rift propagation with (a) air temperature and (b) sea-ice concentrations for the period of October to early-April (Figs. 2,3) between 2003 and 2022.

(a) Air temperature

Daily mean near-surface (2 m) air temperature data were extracted for all austral summers between 2003 and 2022, which is provided at a 0.25 degree (30 km) from ERA5 reanalysis data (Hersbach and others, 2023). To understand the link between rift propagation and temperature, we calculated the positive degree-days (PDDs) using mean degree-hour method (Day, 2006). PDD is defined as the total sum of hourly averaged temperatures per day above 0°C. The PDDs were summed over each season, and we analysed whether there was a significant correlation between PDD and rift propagation rate.

(b) Sea- ice concentration

Sea-ice concentration data were extracted from Nimbus-7 SMMR and DMSP SSM/I-SSMIS Passive Microwave Data V002 (DiGirolamo and others, 2022). This region includes multi-year sea ice and mélange that fills the rift openings. The spatial resolution of the sea ice concentration dataset is 25 km. As sea-ice concentration and rift lengths both have strong seasonal signals, a linear regression was performed to understand if changes in sea-ice concentration influences the propagation rate (Walker and others, 2015). To directly compare the variability in sea ice concentration with rift propagation rates, the seasonal component of sea-ice concentration was first removed.

4. Results

4.1. Ice front position

Our earliest images date from 1963 and 1973 and confirm that a large calving event occurred between these dates, resulting in around 60 km of retreat (Fig. 4). Our analyses indicate that the ice front gradually advanced between 1973 and 2022 and that it is currently around 30 km landward from its near maximum extent prior to the calving event in 1967. Furthermore, there is little evidence that the shape of the ice front has exhibited any major change between 1973 and 2022 (Fig. 4), suggesting no major calving events have taken place over this period. In addition, the ice front advance rate showed limited changes with an average of $\sim 740 \text{ m yr}^{-1}$ between 1985 and 2022, albeit with small interannual variations in the ice front advance rate (Fig. S1).

At the smaller Jutulstraumen east outlet, the ice front retreated by $\sim 2.3 \text{ km}$ between 1987 and 2000, followed by a slight advance of $\sim 1 \text{ km}$ between 2000 and 2002, a large retreat of $\sim 10 \text{ km}$ between 2002 and 2007, and with a further re-advance of $\sim 6 \text{ km}$ between 2007 and 2022 (Figs. 4c, d).

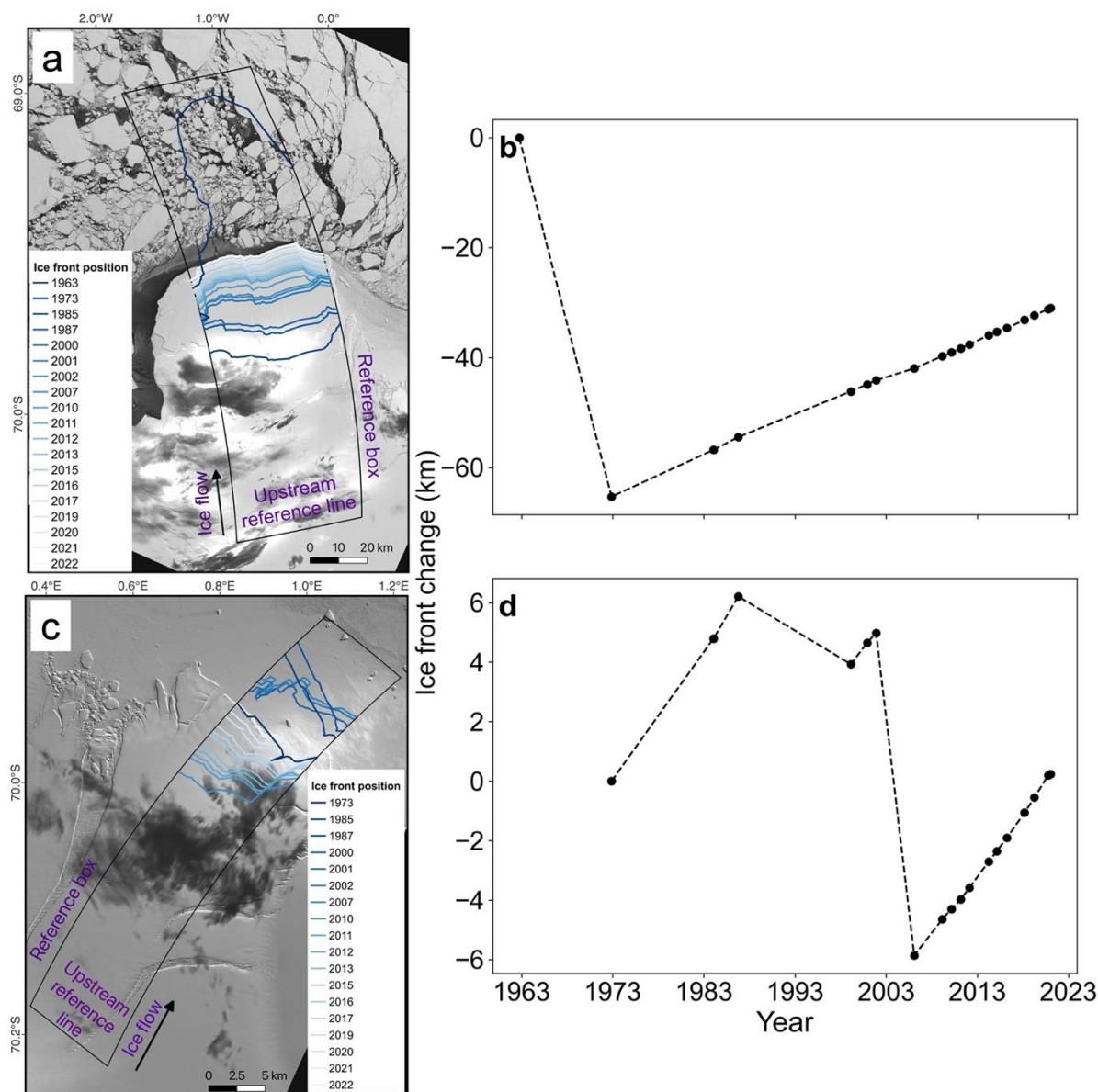


Fig. 4: (a) Mapped ice front position of the main tongue of Jutulstraumen between 1963 and 2022. (b) Ice front position change of Jutulstraumen's main tongue during 1963–2022 from the black curvilinear box delineated in (a). (c) Mapped ice front position of the eastern extension of Jutulstraumen between 1973 and 2022 (d) Ice front position change of eastern extension of Jutulstraumen during 1963–2022 from the black curvilinear box delineated in (c). The background image in (a) and (c) is a Landsat-8 image from 13 October 2021. Note that the errors are too small to be visible at this scale but see Table S1.

4.2. Glacier velocity

The glacier velocity trend along the floating ice tongue showed little overall change between 2000 and 2021, with only minor interannual fluctuations (Fig. 5). As a result, the mean annual velocity was estimated at $\sim 720 \pm 66 \text{ m yr}^{-1}$ across all sampling boxes over the floating ice tongue. This estimated glacier velocity is consistent with the mean rate of advance described in the previous section, which

we calculate as around 740 m yr^{-1} , albeit with some minor fluctuations between 1985 and 2022 (Figs. 5,S1). The mean velocity is in the same range at DT, UT and GL, but is much less at box AGL (Figs. 2,5). The associated uncertainties ranged from ± 0.5 to $\pm 163 \text{ m yr}^{-1}$ (Fig. 5). Although we observed a 10% increase in velocity at UT between 2011 and 2012, the absolute value of increase (55 m yr^{-1}) is smaller than the associated error ($\pm 118 \text{ m yr}^{-1}$). In addition, the 15% decrease in velocity at AGL between 2008 and 2009, with an absolute velocity decrease of 61 m yr^{-1} is smaller than the associated error of $\pm 62 \text{ m yr}^{-1}$.

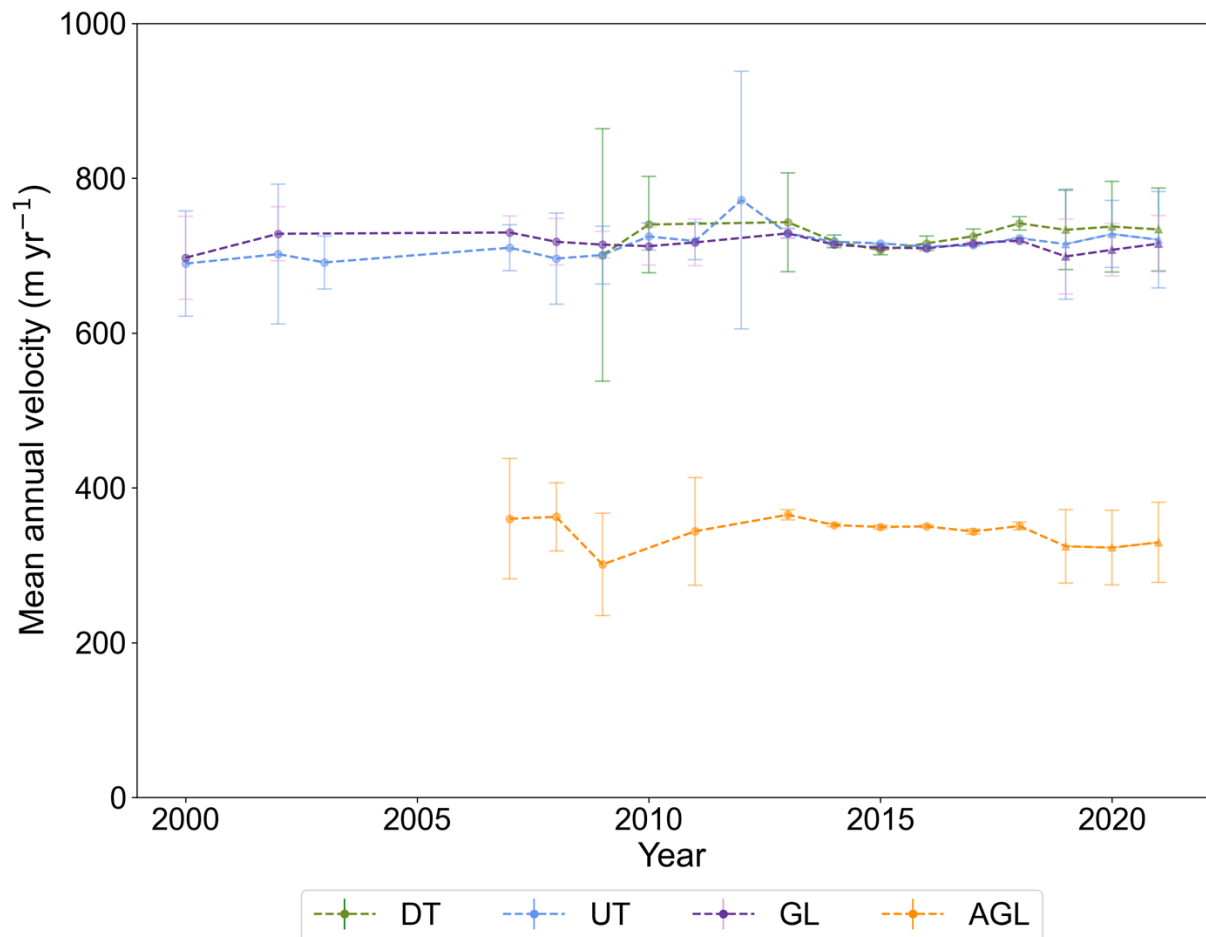


Fig. 5: Trends of mean annual velocity extracted from Jutulstraumen at the four locations at down-ice tongue (DT), up-ice tongue (UT), grounding line (GL) and above the grounding line (AGL) (see Fig. 2 for location). Velocity is extracted from ITS_LIVE (circle) and ENVEO (triangle) velocity mosaics between 2000 and 2021 (Gardner and others, 2019; ENVEO and others, 2021).

4.3. Elevation change

Our results indicate that elevation change trends obtained from Schröder and others (2019) and Nilsson and others (2022) are less comparable and associated with higher uncertainties pre-2003, with notably inconsistent trends between 1992 and 2003 at all sample locations (20, 60, 80, and 120 km inland of GL). However, a general agreement between the two datasets is observed after 2003, with a clear thickening trend of the grounded ice observed from around 2003. It is also worth noting

that both datasets manifest some interannual variability (Fig. 6). Nonetheless, we observed an overall thickening when averaged across all sampling boxes, at a rate of $+0.11 \pm 0.1 \text{ m yr}^{-1}$ between 2003-2017 (Schröder and others, 2019) and $+0.14 \pm 0.04 \text{ m yr}^{-1}$ between 2003 and 2020 (Nilsson and others, 2022) upstream of the grounding line. Furthermore, a similar pattern of thickening of the grounded ice is also observed in the dataset provided by Smith and others (2020) with an average rate of $+0.17 \pm 0.005 \text{ m yr}^{-1}$ (Table S3).

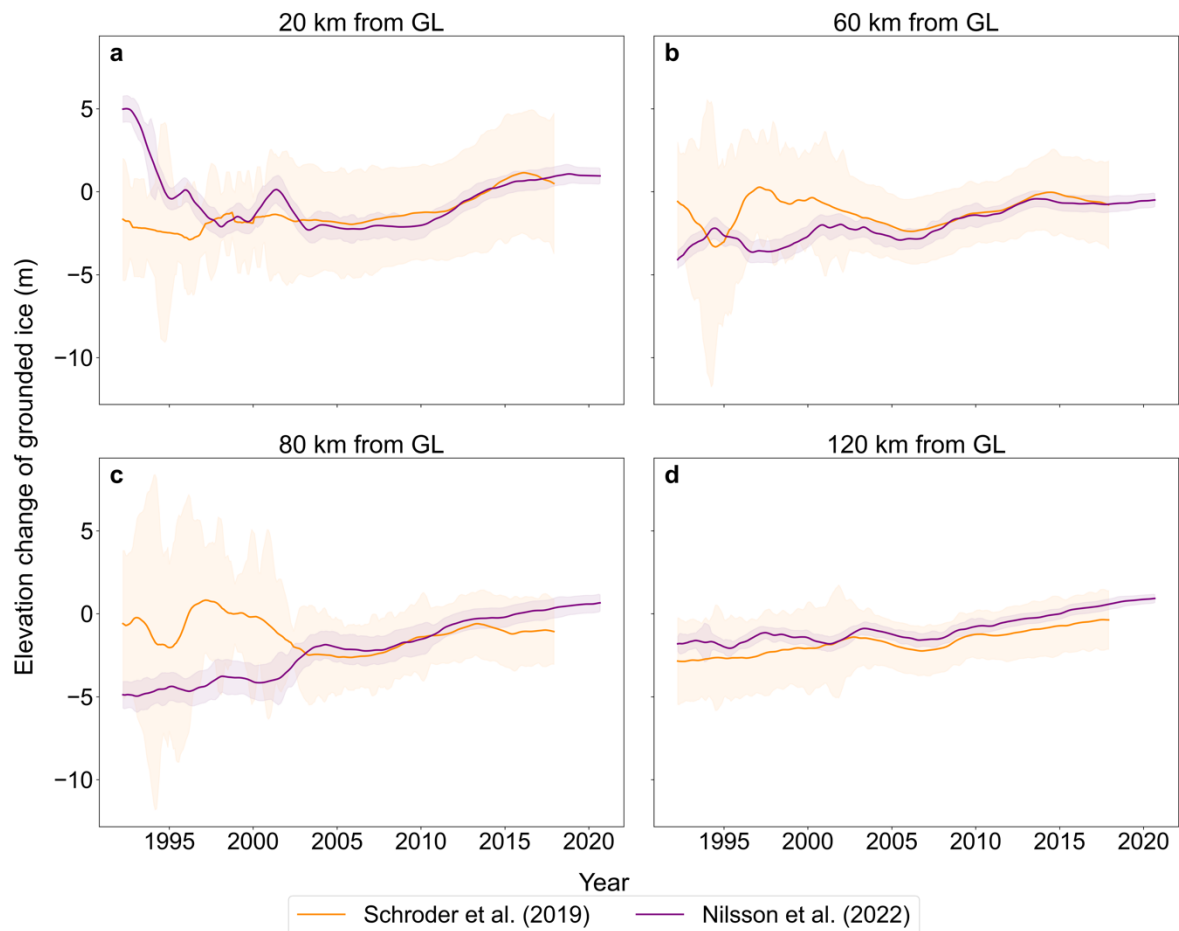


Fig. 6: Monthly elevation changes of the grounded ice observed at four locations, i.e., (a) 20 km, (b) 60 km, (c) 80 km and (d) 120 km inland from the grounding line (GL) at Jutulstraumen between 1992 and 2020, obtained from Schroder and others (2019) and Nilsson and others (2022). The solid lines represent 5-year moving averages and the shaded area represents the corresponding error propagation.

4.4. Grounding line

In this section, we present a comprehensive compilation of all available grounding line positions, categorised according to the two primary methodologies of determining grounding line position detailed in section 3.4. Fig. 7a shows the grounding line positions acquired using DInSAR. Notably, the DInSAR-derived data for Jutulstraumen in 1994 are provided by both MEaSURES (4/3/1994) and AIS CCI (derived from double differences of three subsequent images: (4/3/1994, 7/3/1994,

10/3/1994) coinciding on the same date. The grounding line positions from these two datasets for 1994 align closely.

More recently, the dataset provided by Mohajerani and others (2021), which also used DInSAR data as input for a fully convolutional neural network, includes clusters of grounding line positions (green) and pinning points (yellow) for 2018. Note that within the cluster that is furthest upstream, there are some grounding line positions that correspond to the flexure location or the hinge line, F (Fricker and Padman, 2006; Fricker and others, 2009; Friedl et al., 2020) and these align closely with the 1994 grounding line positions provided by MEaSURES (Rignot and others, 2016) and the AIS CCI (Fig. 7). This overlap at the flexure location suggests a consistency between the three datasets. Meanwhile, other grounding line positions within this cluster are associated with localised features of the grounding zone such as pinning points (Fig. 7). Overall, this suggests limited or no change in grounding line position over the 24-year period between 1994 and 2018.

Fig. 7b shows the grounding line position determined by previously published manual delineations of the break-in slope, I_b (ASAID and MOA) and of the assumed local elevation minimum, I_m , mapped in this study. The ASAID and MOA grounding line positions were digitised at similar locations, showing limited change over time. However, the grounding line positions obtained in this study exhibits a slow advance of ~ 200 m (~ 6 m yr⁻¹ on average) between 1990 and 2022 (Fig. 7b).

Fig. 7c compares the manually delineated grounding line positions (ASAID, MOA, this study) with the earliest available grounding line positions derived from DInSAR (MEaSURES). It is evident from Fig. 7c that the grounding line positions obtained from MEaSURES and AIS CCI which identifies the landward limit of the ice flexure caused by tidal movement (F), are consistently located much further up the ice tongue compared to those obtained from manual delineation of break-in slope, I_b (ASAID, MOA) and the local elevation minimum, I_m (this study). For example, the 1994 DInSAR-derived grounding line position is ~ 18 km upstream from the 1993 grounding line position (I_m) identified in this study. Similarly, the furthest upstream grounding line position from the 2018 DInSAR-derived cluster provided by Mohajerani and others (2021) is ~ 16 km upstream of the 2018 grounding line position identified in this study. This clearly emphasises that grounding line positions acquired using different methods are not directly comparable as they are recording different features of the grounding zone (Fricker and Padman, 2006; Fricker and others, 2009; Friedl et al., 2020; Picton and others, 2023). However, taken together, there is little evidence for a major change in grounding line position at Jutulstraumen (Fig. 7c), although our manually digitised method suggests there may have been a very small (~ 200 m) advance, with approximately ± 100 m uncertainty associated with it (see white to blue lines in Fig. 7b).

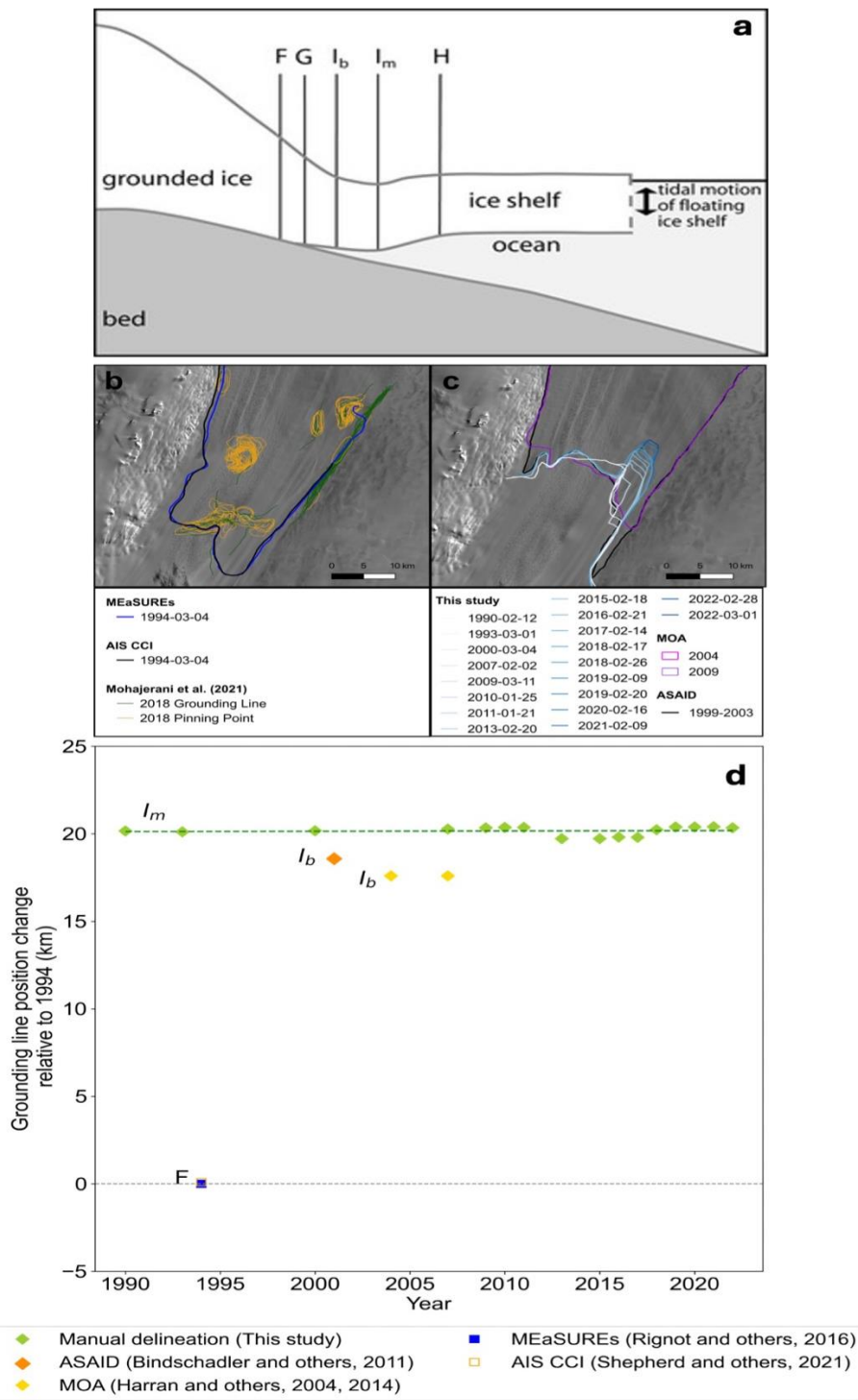


Fig. 7: Grounding line position change of Jutulstraumen based on different GL datasets. (a) Schematic illustration of grounding zone features from Fricker & others (2002) (b) Grounding line position based on vertical motion at the floating part using DInSAR data (MEaSURES, AIS CCI and Mohajerani and others, 2021). (c) Grounding line position based on manual delineation of break-in slope (ASAID, MOA, this study). (d) Change in grounding line position relative to observed 1994 position from all datasets.

4.5. Structural glaciology

The features on Jutulstraumen ice tongue, based on the criteria in Table 2, are displayed in Fig. 8. The western side of the ice tongue has previously been observed to be heavily rifted (cf. Humbert & Steinhage, 2011). Several distinct rifts filled with sea ice/mélange have lengthened during the observation period, predominantly on the western side, with additional rifts forming and expanding on the eastern side near Jutulgryta (Figs. 2, 8). The western side also shows a consistent area of fracture traces, with a slight increase in these features noted over the study period (Fig. 8). Moreover, a surface crevasse field is located near Ahlmannryggen on the western side, with a smaller crevasse field on the eastern side near Jutulgryta (Figs. 2, 8, Humbert & Steinhage, 2011). A mélange zone has been observed between the western crevassed field and Ahlmannryggen. Additionally, during our observation period (1986 to 2022), rifts at the ice front have continued to propagate, leading to small calving events on both the western and eastern margins of the ice tongue (Fig. 9)

Whilst we do not attempt to quantify changes in all the features identified here (Fig. 8), we recognise and quantify 15 of the largest rifts propagating into the ice stream from the ice front which may later play an important role in future calving events.

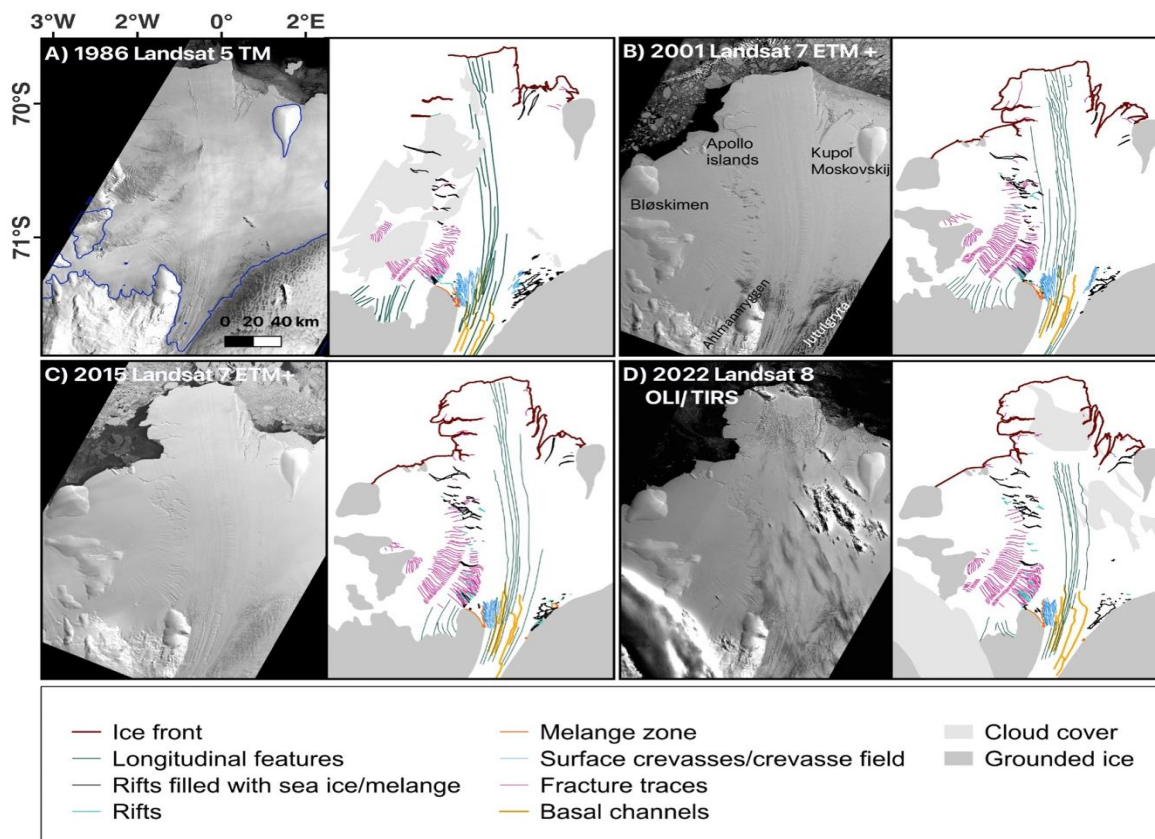


Fig. 8: Structural evolution of Jutulstraumen illustrating widespread rifting from 1986 to 2020. Increased rifting is apparent in the western side of the glacier. The dark blue line in the 1986 satellite image is the MEASUREs grounding line v2 (Rignot and others, 2017).

4.5.1. Rift propagation and links to environmental variables

We examine seven major rifts on the western and eight on the eastern margin of Jutulstraumen (Fig. 3) using satellite imagery (MODIS) from 2003 to 2022. Note that these rifts appear to be a consequence of the ice shelf interaction with the topography near the ice front. For example, the rifts on the west appear to be related to re-activation of pre-existing fractures as the ice pulls away from the headland. On the eastern margin, however, the rifts appear to be associated with the ice shelf's detachment from the ice rise (Kupol Moskovskij) at the front of the glacier. Overall, during the study period, most of these rifts lengthened during the austral summer and there was minimal change during the austral winter. Furthermore, in some seasons, the rift length at the beginning of austral summer was lower than the end of previous summer. This could be due to rift 'healing', snow accumulation at the rift tip, or the presence of sea ice/mélange in the rift cavity resulting in a lower estimation of rift length. Nevertheless, the 19-year timeseries compiled from MODIS imagery shows an overall increase in the lengths of all the rifts measured at different propagation rates (Table S4, S5, Fig. 10). Fig. 10 shows seasonal variation in rift propagation superimposed on a multi-year linear trend.

All seven rifts monitored at the western side of Jutulstraumen exhibited increases in length, with periods of short-term decrease, at an overall long-term average rate of $\sim 2.4 \text{ m d}^{-1}$ from 2003 to 2022. In comparison, rifts on the eastern margin propagated at a slightly slower rate of $\sim 0.7 \text{ m d}^{-1}$. As they lengthened on the eastern margin, rift widening was also observed. For example, rift RE5, which formed around 1986, widened by $\sim 3 \text{ km}$ between 2003 and 2022 ($\sim 0.4 \text{ m d}^{-1}$) and consequently opened-up towards the ocean and filled with sea ice/mélange (Fig. 3a). On the western margin, RW4 had the fastest long-term propagation rate ($\sim 8 \text{ m d}^{-1}$) while RW2 had the slowest rate ($\sim 0.2 \text{ m d}^{-1}$; Fig. 10, Table S4). On the eastern margin, RE8 had the fastest long-term rate ($\sim 3.2 \text{ m d}^{-1}$), while RE1, RE2 and RE7 had the slowest rate ($\sim 0.1 \text{ m d}^{-1}$; Fig. 10, Table S5). The highest propagation rates have been documented in those rifts that are relatively short-lived.

We find that most rift propagation rates tend to slow with time. For instance, the rates during 2003-2011 were higher than those between 2012 and 2022, specifically for RW1 (2003-2011: 3.1 m d^{-1} and 2012-2022: 0.3 m d^{-1}) and RW2 (2003-2011: 0.9 m d^{-1} and 2012-2022: 0.1 m d^{-1}). In addition, smaller rifts exhibited higher propagation rates. On the western margin, RW4 and RW5 showed propagation rates of approximately 8 m d^{-1} and 1.6 m d^{-1} , respectively, until the calving event in 2011 (Table S4), when a small part ($\sim 183 \text{ km}^2$) of the ice front calved off (Fig. 9a). Similarly, the rifts RE6 and RE7 propagated at $\sim 1.4 \text{ m d}^{-1}$ and $\sim 0.1 \text{ m d}^{-1}$ from 2003 until a calving event in 2006 (Table S5), when a small part ($\sim 128 \text{ km}^2$) of the ice front calved off (Fig. 9b).

Note that, on the western margin, RW3 (yellow) was observed until 2011 when a small part calved off and the remaining fragment of RW3 was re-named as RW6 (violet) (Fig. 10a). On the eastern margin, RE3 (green) and RE4 (light pink), which were separate until 2009, merged in the latter half of 2009 and were renamed as RE3+RE4 (brown) (Fig. 10b).

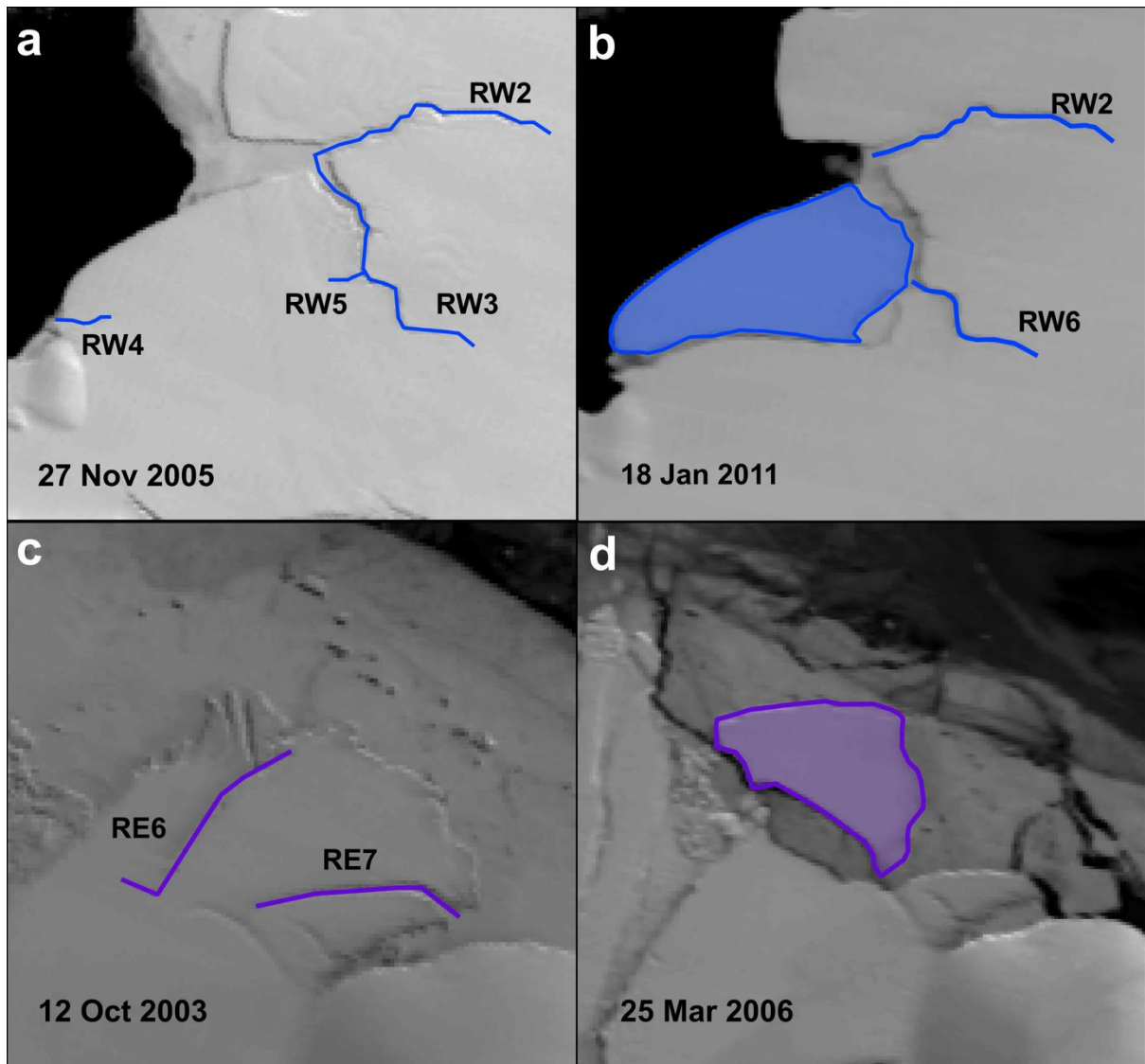


Fig. 9: (a) Shows the calving of a small part on the eastern margin of Jutulstraumen between 27 November 2005 and 18 Oct 2011 due to propagation of rifts RW4 and RW5. (b) Shows the calving of a small part on the western margin of Jutulstraumen between 12 October 2003 and 25 March 2006 due to propagation of rifts RE6 and RE7.

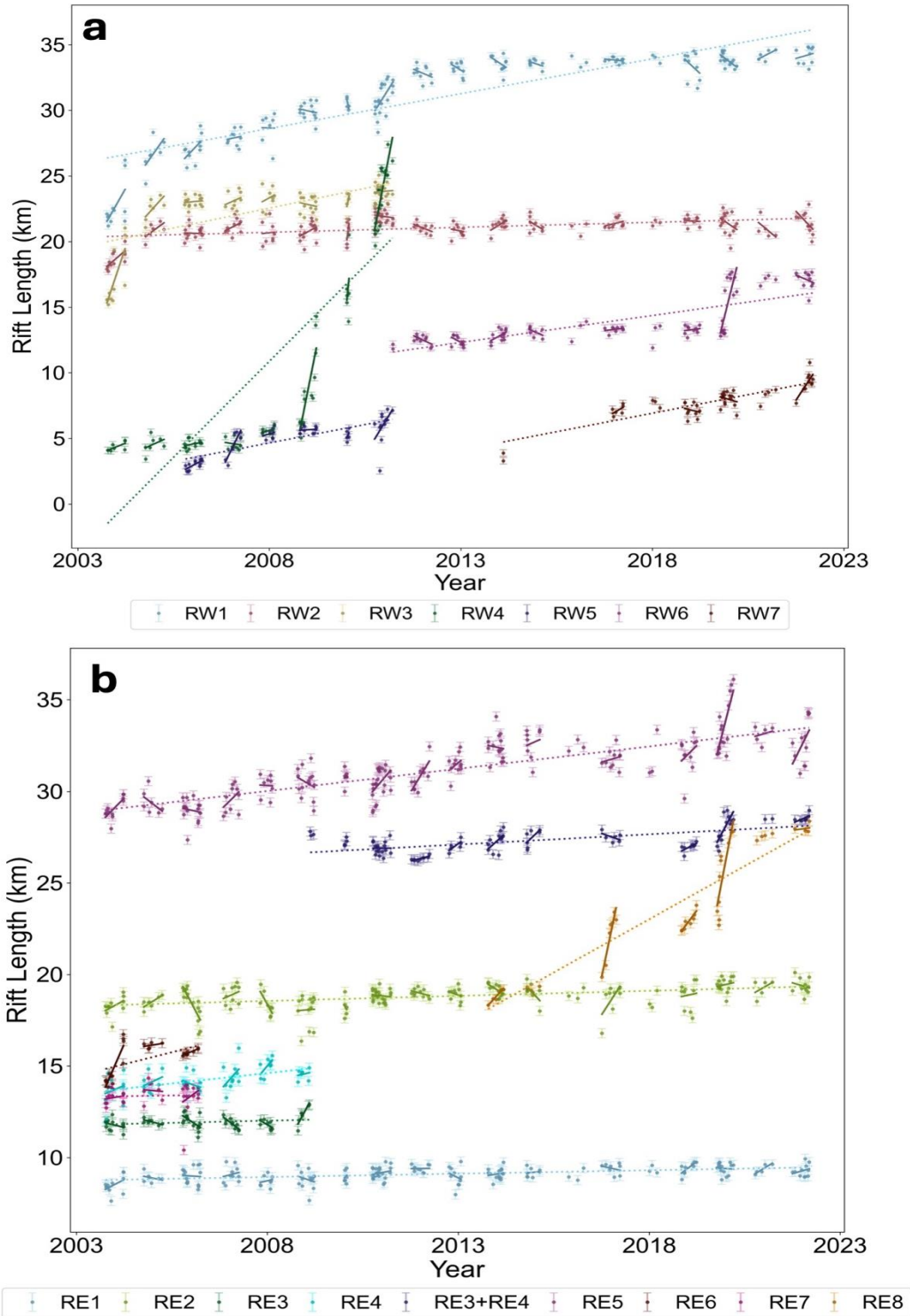


Fig. 10: Measured rift lengths derived from MODIS imagery between 2003 and 2022 on the (a) western side and (b) eastern side of Jutulstraumen. The error bars represent 1 pixel, where pixel size for MODIS is 250 m. MODIS times series for RW1 to RW7 and RE1 to RE8 with linear regression analysis. Solid lines show the linear regression performed to estimate slopes for each summer season for each rift (Case A, Table S4, S5). Dashed lines denote a linear fit applied to the entire dataset of rift lengths for each rift (Case C, Table S4, S5) (see Section 3.5).

The patterns of rift propagation have been observed to be highly variable, ranging from 0 m d^{-1} to 100 m d^{-1} , within each austral summer season (Fig. 10). The regression analysis determined that the propagation rates for each summer season were significantly different from each other between 2003 and 2022 at 95% confidence interval (Table S4, S5). In addition, the differences between rift length at the end and beginning of austral summer were mostly less than one pixel ($<250 \text{ m}$), with instances of rift healing also observed, indicating minimal rift propagation during winter period (Walker and others, 2015). For Case C, the linear fit applied to the entire dataset showed variable rift propagation rates, as detailed in Tables S4 and S5. This analysis underlines the complex and variable nature of rift propagation rates.

Further analysis of factors that influence rift propagation rates reveals that the relationship between these rates and environmental conditions have no significant correlation (see Figs. S3-S6). The 2 m air temperature observed over the sample box, covering the fast-flowing part of the glacier (Fig. 2), varied during austral summer (October-early April), ranging from -35°C to 4°C . Air temperatures typically peaked soon after late December and the PDDs typically occurred between December and February (Figs. S2a, b). We tested whether the seasons with highest propagation rate coincided with high PDD periods and *vice versa* but, no statistically significant correlation is detected between the two variables at 95% confidence interval (e.g. for RW1, correlation coefficient = 0.02). In fact, while some rifts exhibited a weak positive correlation with PDD, others showed a weak negative correlation (Figs. S3, S4). This observation suggested that PDDs are not a factor driving rift propagation at Jutulstraumen (Figs. S3, S4).

Similarly, no significant correlation was observed between sea ice concentration and rift propagation rates. Sea-ice concentration over each austral summer exhibit some interannual variability but the maximum sea-ice concentration was observed between October to November after which it starts to decrease to its minimum value in late January or early February (Fig. S2c). It was observed that rift propagation begins in late October when sea-ice concentration is close to its maximum. We tested whether higher rift propagation rates tended to occur during low sea-ice concentration seasons and *vice versa* (Figs. S5, S6) and find that rift propagation rate shows no significant correlation with sea-ice concentration (e.g. for RW2, correlation coefficient = 0.01). Indeed, some rifts displayed a weak positive correlation with sea ice concentration while others exhibited a weak negative correlation. Although our analysis did not detect correlations at the seasonal scale for either air temperature or sea ice concentrations, we cannot rule out that such relationships might exist at higher temporal resolutions (e.g., daily or weekly).

5. Discussion

5.1. Little change in ice dynamics at Jutulstraumen over the past 60 years

Taken together, our observations indicate minimal dynamic change on Jutulstraumen over the last six decades, with the key findings indicating a steady advance of the main ice tongue ($\sim 740 \text{ m yr}^{-1}$), limited change in ice velocity ($\sim 720 \pm 66 \text{ m yr}^{-1}$), small average thickening of grounded ice across the catchment ($\sim +0.14 \pm 0.04 \text{ m yr}^{-1}$), and no obvious change in grounding line position, other than a possible advance of around 200 m , albeit with large uncertainties ($\sim \pm 100 \text{ m}$).

Between 1973 and 2022, the ice front advanced at an average rate of $\sim 740 \text{ m yr}^{-1}$ with limited change in geometry. Currently, the ice front is $\sim 30 \text{ km}$ behind the maximum extent of the ice front in 1960s, just before it underwent its last major calving event (Fig. 4a). This suggests that it will take nearly ~ 40 years for the ice front to reach its previous maximum extent, considering the current ice front advance rate.

The average ice flow velocity remained consistent throughout the observation period. This could be largely influenced by the pinning points flanking Jutulstraumen coupled with high strain rates arising from the presence of the western rift system and lateral stress from the bounding mountain topography (west: Ahlmannryggen and east: Jutulgryta) near the grounding line (Fig. 2, Humbert & Steinhage, 2011; Mas e Braga and others, 2023), along with a cold-water regime. The steady velocity may also be partly attributed to the presence of large 'passive' frontal areas in Fimbulisen (Fürst and others, 2016). This 'passive' frontal area, also known as 'passive shelf ice' (PSI), refers to a portion of the floating ice shelf which, upon removal, is expected to have little to no dynamic impact. The PSI for the Jelbart-Fimbulisen area was estimated to be 17.1%, indicative of a 'healthy' PSI portion (Fürst and others, 2016). A higher percentage of PSI is important because any loss of this passive ice does not significantly affect ice velocity. In addition, during the study period, there were no major changes in the configuration of the Fimbulisen. The combination of a large PSI fraction and a stable ice shelf configuration might well account for the velocity observed throughout the study period.

Additionally, analysis of elevation change of grounded ice highlights an overall pattern of thickening, particularly after 2003, with an average rate of thickening estimated at $+0.14 \pm 0.04 \text{ m yr}^{-1}$ between 2003 and 2020 (Nilsson and others, 2022). The observed trend could be attributed to a series of high accumulation events in DML that occurred between 2001 and 2006 (Schlosser and others, 2010) and during the winter season from 2009 to 2011 (Lenaerts and others, 2013). This event resulted in an increased mass balance of around $+350 \text{ Gt}$ along the coast of DML (Boening and others, 2012; Groh & Horwath 2021). Additionally, the 2009-2011 high precipitation event over DML has been predicted to be part of a long-term trend (Frieler and others, 2015; Medley and others, 2018), but it is important to note that the predicted rates of increase in both temperature and snowfall from climate model simulations are relatively low (Medley and others, 2018). This suggests that DML could maintain its current trend of mass gain, barring any major climatic or oceanic shifts that could alter future snowfall patterns or increase basal melt rates.

The minimal changes in ice dynamics are consistent with the grounding line positions observed in this study between 1990 and 2022, which appears to have undergone very little change or possibly a very minor advance. However, discrepancies arise when comparing different datasets and methodologies, as different methodologies capture distinct features within the several-kilometer-wide grounding zone, where the transition from fully grounded to floating ice takes place. It should be noted that for fast-flowing glaciers like Jutulstraumen, the grounding line positions acquired from manual delineation based on the most seaward observed break-in slope, I_b (ASAID, MOA) and local elevation minimum, I_m (this study) are further downstream than those determined from tidal-induced vertical motion from DInSAR (MEaSURES, AIS CCI and Mohajerani and others, 2021). For example, when examining the grounding line positions that are closest in time but acquired from different

methods, the 1993 position obtained in this study using manual delineation is around 18 km downstream from the 1994 MEaSURES and AIS CCI grounding line position.

When we instead consider the relative change in grounding line position indicated via each method, analysis of DInSAR-derived grounding line positions indicates little to no change between the 1994 position (MEaSURES and AIS CCI), and the furthest upstream grounding line position from the 2018 cluster provided by Mohajerani and others (2021). In addition, the proximity of the grounding line positions derived from manual delineation of break-in slope provided by ASAIID (1999-2003) and MOA (2004 and 2009) also suggests no major change in grounding line position during that period. The grounding line position obtained in this study from optical imagery (Landsat 4-8) between 1990 and 2022 indicated only a very minor advance of ~ 200 m (~ 6 m yr⁻¹), with uncertainties of $\sim \pm 100$ m. Interestingly, this estimated rate of advance is broadly in agreement with the rate reported by Konrad and others (2018) at $\sim 2.4 \pm 1.9$ m yr⁻¹ between 2010 and 2016, using surface elevation from CryoSat-2 and bed elevation from Bedmap2 between 2010 and 2016. Thus, although there are major discrepancies between the different methods, each method appears to show very little change over the study period, or with only a very minor advance.

In summary, the relative stability of Jutulstraumen is likely due to the stable configuration of its floating ice tongue and Fimbulisen, which have undergone no major calving events and is associated with low basal melt rate (~ 1 m yr⁻¹) (Langley and others, 2014) linked to the presence of cold Eastern Shelf water (Hatterman and others, 2012). Additionally, the velocity could be stabilised by the suture zone on the western margin of Jutulstraumen, linked to the pinning points at the ice front and lateral stress from bounding mountain topography near the flux gate (Fig. 2, Humbert & Steinhage, 2011; Mas e Braga and others, 2023). That said, recent observations have raised concerns about a slight increase in basal melting of around 0.62 m yr⁻¹ between 2016 and 2019 (Lauber and others, 2023). This increase has been linked to the incursion of pulses of WDW resulting from reduced sea ice and stronger subpolar westerlies associated with a positive SAM (Lauber and others, 2023). Furthermore, the evidence of very slight thickening upstream of the grounding line and minor grounding line advance suggests little sign of a dynamic imbalance in Jutulstraumen. Moreover, the limited change in ice discharge, estimated at 30 ± 2.2 Gt yr⁻¹ between 2009 and 2017, along with total mass gain of +33 Gt between 1979 and 2017 as reported by Rignot and others (2019), also suggests Jutulstraumen is currently not out of balance and may even be gaining mass slightly (The IMBIE team, 2023), which is consistent with our suite of observations.

5.2. Structural evolution

The analysis of the structural glaciology has identified that Jutulstraumen has several large surface features that may influence the structural stability of the glacier in the future (Fig. 8). Notably, the western rift system, comprising of fractures, fracture traces, rifts filled with sea ice/mélange, and crevasse fields (Fig. 8), primarily formed due to shear stresses generated between different flow units, specifically the fast-moving central trunk and the slow-moving lateral margin of the ice stream (Humbert & Steinhage, 2011; Fig. 2). The persistent presence of fracture traces in the western rift system suggests that these features have gradually developed and evolved as ice passes over an ice

rumple, propagating both laterally and vertically (Humbert & Steinhage, 2011). However, the fracture traces could also represent surface expressions of basal crevasses (Fig. 8) as suggested by Humbert and Steinhage (2011), Luckman and others (2012) and McGrath and others (2012). Such fracture traces or surface expressions of basal crevasses may have facilitated the initiation and evolution of rifts further downstream towards Apollo Island (Figs. 2, 8), which could potentially weaken the structural integrity of the glacier.

The rifts measured at the ice front do not originate from the ice stream itself but appear to propagate into it near the margin. The observed temporal pattern of rift propagation is complex, exhibiting large seasonal and interannual variability. The long-term rift propagation rates range from around 0.1 to 8 m d⁻¹, with differences in propagation rates on the western and eastern margins of the ice tongue. The rifts on the eastern margin tend to propagate at a slower long-term summer average rate than the rifts on the western margin. This variability in rift propagation rates may be attributed to the direction of flow of the ice-tongue, which curves towards west. This curvature influences the formation of rifts on the eastern margin as ice detaches from the ice rise, Kupol Moskovskij, near the ice front (Figs. 2, 3). Consequently, rifts such as RE5 on the eastern margin tend to expand in width and propagate at a slower rate. It is possible that as a rift widens, the stress concentrated at the rift tip, which generally drives rift lengthening, is redistributed across a wider area of the rift wall. This redistribution of stress at the rift tip might temporarily reduce the tensile stress driving rift lengthening (Bassis and others, 2007, 2008; Glasser and others, 2009). In contrast, the rifts on the western margin appear to be related to re-activation of pre-existing fractures as the ice pulls away from the Apollo Island (Figs. 2, 8). Therefore, the calving regime could be influenced by the adjacent flow units, defined as neighbouring sections of the glacier or ice shelf characterised by varying flow velocities. The fast-flowing ice stream in the middle interacts with the slower moving ice on either side of the ice stream, generating shear stress, which could further influence the formation and propagation of these rifts.

In addition, previous studies have suggested that sea ice concentration or ice mélange can play an important role in rift propagation. When sea ice is absent in rift openings, there is an extended period of exposure to open ocean conditions and ocean swells. This exposure potentially impacts the rate at which rifts propagate, leading to calving and eventual disintegration of ice shelves, as observed in the Larsen A, B, and Wilkins ice shelves (Massom and others, 2018; Larour and others, 2021). Prior research has also linked the disintegration of ice shelves to increasing atmospheric temperatures (Mueller and others, 2008). However, using linear regression analysis, we can confirm that high rift propagation rates at Jutulstraumen are not related to high air temperatures at seasonal scale (Figs. S3, S4). This finding is supported by previous studies showing that despite a warmer-than-average condition during the winter of 2007, the Amery and West Ice Shelves in East Antarctica saw a decrease in rift propagation rates, and rift activity came to a complete halt in the following austral summer in the Shackleton Ice Shelf (Walker and others, 2013). Whilst during a relatively colder winter in 2005, three rifts (rifts W2, T1 and T2) in the Amery ice shelf actively propagated, indicating a complex, non-linear link between temperatures and rift activity on these shelves (Walker and others, 2013).

Similarly, the correlation between rift propagation rate and sea-ice concentration at Jutulstraumen is also not statistically significant at 95% confidence level, indicating that lower sea-ice concentration does not necessarily lead to higher rift propagation rates. This finding aligns with previous research on the Amery Ice Shelf in the EAIS, where studies have consistently found no statistically significant correlation between environmental factors like air temperature or sea-ice concentration and rift propagation rates (Fricker and others, 2005; Bassis and others, 2008; Walker and others, 2015). In addition, ice shelves such as Larsen C, Ronne and Filchner, adjacent to the Weddell Sea and characterised by year-round high sea ice levels, have not exhibited decreased rift activity during periods of high sea ice concentration. This is unlike the behaviour observed in the Larsen A, B and the Wilkins ice shelves where a clear relationship between sea ice and rift propagation has been observed. These ice shelves experienced a notable increase in rift lengthening during periods with no sea ice buffer. This reduced buttressing from sea ice and prolonged exposure of the water-filled rifts to the ocean swells, led to calving and eventual disintegration of the ice shelves (Massom and others, 2018).

In summary, we expect the rifts observed on Jutulstraumen to continue to propagate regardless of the ice shelf-scale changes in environmental parameters (particularly, temperature and sea ice concentration). On a more regional scale, factors like the presence or absence of sea ice/mélange in rift openings or wind-blown snow/ice might impact rift propagation rates, although the lack of detailed sea ice data complicates this assessment (MacAyeal and others, 1998; Khazendar & Jenkins, 2003; Larour and others, 2004; Fricker and others, 2005; Walker and others, 2013). Nevertheless, our analysis shows that over the observation period the rifts propagate at a relatively steady rate (Fig. 10).

Additional factors that may impact rift propagation rates could be arrival of tsunamis, as observed in Amery Ice Shelf between 2002 and 2012, following which large rift propagation events occurred (Walker and others, 2015). Moreover, mechanical/tidal interaction between the ocean and ice shelf, especially since these rifts open towards the ocean (Walker and others, 2013), could also contribute to rift propagation. Seasonal variations in rift propagation rates might stem from changing ocean conditions affecting the basal melting beneath the ice shelf. Lauber and others (2023) reported intensified pulses of WDW beneath the ice shelf after 2016, leading to increased basal melt rates. This could influence the ice shelf's structural heterogeneity (e.g., through localised high melt rates in basal channels), further contributing to rift propagation. Alley and others (2022) suggested that basal channels are crucial in determining the basal melt rate, a factor that greatly influences the stability of the ice shelves. Additionally, these channels can affect how and where fractures form and propagate, directly impacting ice-shelf calving. An example of this can be seen in the Pine Island Glacier, where the presence of a basal channel is linked to the formation of both transverse and along-channel fractures (Dow and others, 2018; Alley and others, 2022). The basal channels identified in this study originate near the grounding line, which could influence the expansion of the mélange zone, the propagation of the rifts filled with sea ice/mélange, or formation of new rifts/crevasses in the ice stream (Fig. 8). However, it remains unclear about their influence on the rifts at the ice front. In addition, the presence of marine ice in the suture zones could also impact the structural integrity of

the ice shelf (Walker and others, 2013; Kulesa and others, 2014). Such dynamics have been observed on the Amery Ice Shelf, indicating a multifaceted interplay of environmental and oceanographic factors in rift propagation (Herraiz-Borreguero and others, 2013; Walker and others, 2013; Walker and others, 2015).

Thus, at Jutulstraumen, the advancing of the ice tongue and additional stresses may play a more important role than environmental factors in influencing rift propagation and the next calving event. Therefore, as the Jutulstraumen ice tongue is approaching its maximum extent of 1960s, it is essential to maintain continuous monitoring of these rifts, as they have the potential to influence a major calving event.

5.3. Future evolution of Jutulstraumen

In 2022, Jutulstraumen's ice front was ~30 km behind its previous maximum extent of the 1960s. Given the average rate of advance, it would reach its last maximum extent in ~40 years. However, if we take the long-term average rate of rift lengthening (Figure 10) into the ice stream, this calving event could occur prior to the ice tongue reaching its maximum extent and possibly in as little as 32 years. For instance, if both RW6 (~1.5 m d⁻¹) and RE3+RE4 (~0.3 m d⁻¹) propagate at their average rate, the two rifts will connect in around 32 years, leading to a calving event. This calving event will result in the loss of an iceberg of ~55 km in length, ~65 km in width and ~3575 km² in area. The size of this potential iceberg would exceed the dimensions of the recently calved iceberg A-81 from the Brunt Ice Shelf in January 2023, which was approximately 1550 km² in size. Furthermore, the presence of a deep trough crossing the continental shelf beneath the floating part of Jutulstraumen would provide a pathway for warm water to intrude to the grounding line if ocean circulation were to change in the region (Fig. 1c). This indicates a possibility of connections being made between the projected warming of the Weddell Sea (Golledge and others, 2017) and Fimbulisen/Jutulstraumen. This is similar to the response predicted for the neighbouring Recovery catchment under future warming scenarios by Golledge and others (2017). Modelling also suggests large-scale changes including significant ice surface thinning by 2300 in and around Jutulstraumen under a +3°C air temperature warming scenario (DeConto and others, 2021). Despite a relatively minor current response to changing climate and ocean conditions, it is essential to monitor changes in Jutulstraumen to identify early warnings of dynamic imbalance in the next few decades, particularly given that it drains a significant portion of East Antarctica.

6. Conclusion

This study has shown that Jutulstraumen has exhibited limited change in ice dynamics over the observation period between 1960s and 2022, with no signs of any dynamic imbalance. Following the significant calving event in 1967 (see van Autenboer & Decler, 1969; Vinje, 1975; Swithinbank and others, 1977; Kim and others, 2001), the ice front has advanced steadily at ~740 m yr⁻¹ (1973-2022). The velocity has been largely consistent between 2000 and 2021 at ~720 ± 66 m yr⁻¹ with minimal thickening of the grounded ice at ~+0.14 ± 0.04 m yr⁻¹ across the catchment (2003-2020). The grounding line has shown no obvious change and may have slowly advanced between 1990 and

2022 ($\sim 6 \text{ m yr}^{-1}$) based on manual delineation in this study. Taken together, our observations are consistent with the notion that the large ice shelf (Fimbulisen) is modulating the steady ice velocity and stable grounding line location, largely influenced by the drag imposed by lateral pinning points either side of the main ice stream. Such behaviour is also consistent with characteristics of outlet glaciers in cold-water shelf regime, with minimal ice shelf thinning. However, recent observations highlighted the incursion of pulses of WDW beneath the ice shelf, leading to a higher basal melt rate (Lauber and others, 2023). Should such events persist or become more frequent, they could potentially influence the ice dynamics at Jutulstraumen.

The 19-year time series of rift lengths between 2003 and 2022 have indicated that the rifts have been increasing in length and some rifts (RW4 and RW5; RE6 and RE7) have triggered small calving events during the observation period (Fig. 9). The average propagation rates differed for each rift with most exhibiting a seasonal signal of lengthening, but with marked interannual variability. Comparison of rift propagation rates with air temperature and sea-ice concentration suggested that these phenomena were not linked to rift propagation rates at seasonal scale (Figs. S3-S6). Rather, rift lengthening is likely resulting from the continued generation of shear stresses at the lateral margin as the floating ice tongue continues to advance. If the current rate of ice front advance is maintained then the next calving event is likely to occur in around 40 years, based on its position just prior to its last calving event in the late 1960s. However, if the long-term rate of rift lengthening is maintained, then it could take place much sooner and in around 32 years.

7. Data availability

The Landsat imagery used in this study are available from United States Geological Survey EarthExplorer (<https://earthexplorer.usgs.gov/>) and Moderate Resolution Imaging Spectroradiometer (MODIS) imagery are available from NASA's National Snow and Ice Data Center (<https://nsidc.org/data/modis>). The annual ice velocity mosaics from ITS_LIVE are available from NASA's National Snow and Ice Data Center (<https://its-live.jpl.nasa.gov>). The monthly elevation changes products produced by Schröder and others (2019) and Nilsson and others (2022) are available from (<https://doi.org/10.5194/tc-13-427-2019>) and (<https://doi.org/10.5194/essd-14-3573-2022>), respectively. The ice thickness change rate produced by Smith and others (2020) are available from ResearchWorks Archive (<http://hdl.handle.net/1773/45388>). The MEaSURES grounding line data produced by Rignot and others, (2016) are available from <https://nsidc.org/data/nsidc-0498/versions/2>. The grounding line data produced by Mohajerani and others (2021) are available from <https://doi.org/10.7280/D1VD6G>. The AIS CCI grounding line data are available from ENVEO CryoPortal (<http://cryoportals.enveo.at/>). The ASAIID grounding line products (1994-2003) are available at U.S. Antarctic Program Data Center (<https://www.usap-dc.org/view/dataset/609489>). The MOA grounding line products (2004-2009) produced by Harran and others (2005, 2014) are available from NASA's NSIDC at (<https://doi.org/10.5067/68TBT0CGJSOJ>) and (<https://doi.org/10.5067/4ZL43A4619AF>), respectively. The ERA-5 daily 2 m air temperature and is available from <https://cds.climate.copernicus.eu/datasets/reanalysis-era5-single-levels?tab=download>

and the sea ice concentration data were extracted from Nimbus-7 SMMR and DMSP SSM/I-SSMIS Passive Microwave Data V002 (<https://nsidc.org/data/nsidc-0051/versions/2>).

8. Supplementary material

9. Acknowledgement

AS was funded by Durham University Doctoral Scholarship, Durham University. The authors would like to thank the Editor (Bea Csatho), together with Tom Holt and an anonymous reviewer for their constructive comments on this paper during peer review.

10. Author Contributions

AS, CRS and SSRJ designed the initial study. AS undertook the data collection and analysis with guidance from CRS and SSRJ. AS led the manuscript writing, with input from all authors.

11. Conflict of Interest. None

12. References

- Alley KE, Scambos TA, Siegfried MR and Fricker HA (2016) Impacts of warm water on Antarctic ice shelf stability through basal channel formation. *Nat. Geosci.*, **9**(4), 290–293 (doi: 10.1038/ngeo2675)
- Alley KE, Scambos TA, Alley RB (2022) The role of channelized basal melt in ice-shelf stability: recent progress and future priorities. *Ann. Glaciol.*, **63**(87-89), 18–22 (doi: 10.1017/aog.2023.5)
- Bassis JN, Fricker HA, Coleman R and Minster JB (2008) An investigation into the forces that drive ice-shelf rift propagation on the Amery ice shelf, East Antarctica. *J. Glaciol.*, **54**(184), 17–27 (doi: 10.3189/002214308784409116)
- Bassis JN and 7 others (2007) Seismicity and deformation associated with ice-shelf rift propagation. *J. Glaciol.*, **53**(183), 523–536 (doi:10.3189/002214307784409207)
- Bindschadler R and 17 others (2011) Getting around Antarctica: new high-resolution mappings of the grounded and freely-floating boundaries of the Antarctic ice sheet created for the International Polar Year. *The Cryosphere*, **5**, 569–588 (doi: 10.5194/tc-5-569-2011)
- Bindschadler R and Choi, H (2011) High-resolution Image-derived Grounding and Hydrostatic Lines for the Antarctic Ice Sheet U.S. Antarctic Program (USAP) Data Center (doi:10.7265/N56T0JK2)
- Black TE and Joughin I (2022) Multi-decadal retreat of marine-terminating outlet glaciers in northwest and central-west Greenland. *The Cryosphere*, **16**, 807–824 (doi: 10.5194/tc-16-807-2022)
- Boening C, Lebsack M, Landerer F and Stephens G (2012) Snowfall-driven mass change on the East Antarctic ice sheet. *Geophys. Res. Lett.*, **39**(21) (doi: 10.1029/2012GL053316)
- Brancato V and 11 others (2020) Grounding Line Retreat of Denman Glacier, East Antarctica, Measured With COSMO-SkyMed Radar Interferometry Data. *Geophys. Res. Lett.*, **47**(7), e2019GL086291 (doi: 10.1029/2019GL086291)

- Brunt KM, Fricker HA, Padman L, Scambos TA and O'Neel S (2010) Mapping the grounding zone of the Ross Ice Shelf, Antarctica, using ICESat laser altimetry. *Ann. Glaciol.*, **51**(55), 71–79. (doi:10.3189/172756410791392790)
- Christie FDW and 7 others (2018) Glacier change along West Antarctica's Marie Byrd Land Sector and links to inter-decadal atmosphere–ocean variability, *The Cryosphere*, **12**, 2461–2479, (doi: 10.5194/tc-12-2461-2018)
- Christie FDW, Bingham RG, Gourmelen N, Tett SFB and Muto A (2016) Four-decade record of pervasive grounding line retreat along the Bellingshausen margin of West Antarctica. *Geophys. Res. Lett.*, **43**(11), 5741–5749 (doi: 10.1002/2016GL068972)
- Day T (2006) Degree days: theory and application. (CIBSE Technical Memorandum TM41) Chartered Institution of Building Services Engineers, London
- Decleir H and van Autenboer T (1982) Gravity and magnetic anomalies across Jutulstraumen, a major geologic feature in western Dronning Maud Land, Antarctica. *Antarct. Geosci.. 3rd Symposium on Antarctic Geology and Geophysics, Madison*, August 1977, 941–948.
- DeConto RM and 11 others (2021) The Paris Climate Agreement and future sea-level rise from Antarctica. *Nature*, **593**(7857), 83–89 (doi: 10.1038/s41586-021-03427-0)
- DeConto RM and Pollard D (2016) Contribution of Antarctica to past and future sea-level rise. *Nature*, **531**(7596), 591–597 (doi: 10.1038/nature17145)
- Depoorter MA, Bamber JL, Griggs JA, Lenaerts JTM, Ligtjenberg SRM, van den Broeke MR and Mohold G (2013) Calving fluxes and basal melt rates of Antarctic ice shelves, *Nature*, **502**, 89–92, (doi:10.1038/nature12567)
- DiGirolamo N, Parkinson CL, Cavalieri DJ, Gloersen P and Zwally HJ (2022) *Sea Ice Concentrations from Nimbus-7 SMMR and DMSP SSM/I-SSMIS Passive Microwave Data*. (NSIDC-0051, Version 2). [Data Set]. Boulder, Colorado USA. NASA National Snow and Ice Data Center Distributed Active Archive Center (doi: 10.5067/MPYG15WAA4WX) (Accessed on 25-11-2024)
- Dow CF and 8 others (2018) Basal channels drive active surface hydrology and transverse ice shelf fracture. *Sci. Adv.*, **2018**(4), eaao7212.
- ENVEO, Wuite J, Hetzenecker M, Nagler T and Scheiblauer S (2021) ESA Antarctic Ice Sheet Climate Change Initiative 60 (Antarctic_Ice_Sheet_cci): Antarctic Ice Sheet monthly velocity from 2017 to 2020, derived from Sentinel-1, v1. NERC EDS Centre for Environmental Data Analysis [data set] (doi: 10.5285/00fe090efc58446e8980992a617f632f)
- Ferraccioli F, Jones PC, Curtis ML, Leat PT and Riley TR (2005) Tectonic and magmatic patterns in the Jutulstraumen rift (?) region, East Antarctica, as imaged by high-resolution aeromagnetic data. *Earth, Planets, and Space*, **57** (doi: 10.1186/BF03351856)
- Ferrigno JG, Lucchitta BK., Mullins KF, Allison AL, Allen RJ and Gould WG (1993) Velocity measurements and changes in position of Thwaites Glacier/iceberg tongue from aerial photography, Landsat images and NOAA AVHRR data. *Ann. Glaciol.*, **17**, 239–244 (doi: 10.3189/s0260305500012908)
- Ferrigno JG and Gould WG (1987) Substantial changes in the coastline of Antarctica revealed by satellite imagery. *Polar Record*, **23**(146), 577–583 (doi: 10.1017/S003224740000807X)Fogwill CJ

- and 8 others (2014) Testing the sensitivity of the East Antarctic Ice Sheet to Southern Ocean dynamics: Past changes and future implications. *J. Quaternary Sci.*, **29**(1), 91–98 (doi: 10.1002/jqs.2683)
- Fretwell P and 59 others (2013) Bedmap2: improved ice bed, surface and thickness datasets for Antarctica. *Cryosphere* 7, 375–393 (doi:10.5194/tc-7-375-2013)
- Frezzotti M, Cimbella A and Ferrigno JG (1998) Ice-front change and iceberg behaviour along Oates and George V Coasts, Antarctica, 1912–96. *Ann. Glaciol.*, **27**, 643–650 (doi: 10.3189/1998aog27-1-643-650)
- Frezzotti M (1997) Ice front fluctuation, iceberg calving flux and mass balance of Victoria Land glaciers. *Antarct. Sci.*, **9**(1), 61–73 (doi: 10.1017/s0954102097000096)
- Fricker HA, Coleman R, Padman L, Scambos TA, Bohlander J and Brunt KM (2009) Mapping the grounding zone of the Amery Ice Shelf, East Antarctica using InSAR, MODIS and ICESat. *Antarctic Science*. **21**(5), 515–532 (doi:10.1017/S095410200999023X)
- Fricker HA and Padman L (2006) Ice shelf grounding zone structure from ICESat laser altimetry. *Geophys. Res. Lett.*, **33**, L15502 (doi:10.1029/2006GL026907)
- Fricker HA, Young NW, Coleman R, Bassis JN and Minster JB (2005) Multi-year monitoring of rift propagation on the Amery Ice Shelf, East Antarctica. *Geophys. Res. Lett.*, **32**(2), 1–5 (doi: 10.1029/2004GL021036)
- Friedl P, Weiser F, Fluhler A and Braun MH (2020) Remote sensing of glacier and ice sheet grounding lines: A review, *Earth-Science Reviews*, 201 (doi: 10.1016/j.earscirev.2019.102948)
- Frieler K and 8 others (2015) Consistent evidence of increasing Antarctic accumulation with warming. *Nat. Clim. Change*, **5**, 348–352 (doi: 10.1038/nclimate2574)
- Fürst J and 6 others (2016) The safety band of Antarctic ice shelves. *Nat. Clim. Change*, **6**, 479–482. (doi: 10.1038/nclimate2912)
- Gardner AS, Fahnestock MA and Scambos TA (2019) ITS_LIVE Regional Glacier and Ice Sheet Surface Velocities, National Snow and Ice Data Center [data set], (doi: 10.5067/6II6VW8LLWJ7)
- Gardner AS and 6 others (2018) Increased West Antarctic and unchanged East Antarctic ice discharge over the last 7 years. *Cryosphere* 12(2), 521–547 (doi: 10.5194/tc-12-521-2018)
- Gjessing YT (1970) Mass transport of Jutulstraumen ice stream in Dronning Maud Land. *Årbok. Norsk Polar Institute, Oslo*, 227–228 (<https://core.ac.uk/download/pdf/30820531.pdf>)
- Glasser NF and 7 others (2009) Surface structure and stability of the Larsen C ice shelf, Antarctic Peninsula. *J. Glaciol.*, **55**(191), 400–410 (doi: 10.3189/002214309788816597)
- Glasser NF and Scambos TA (2008) A structural glaciological analysis of the 2002 Larsen B ice-shelf collapse. *J. Glaciol.*, **54**(184), 3–16 (doi: 10.3189/002214308784409017)
- Glasser NF and 7 others (2009) Surface structure and stability of the Larsen C ice shelf, Antarctic Peninsula. *Journal of Glaciology*. 2009;55(191):400-410. doi:10.3189/002214309788816597
- Goel V, Matsuoka K, Berger CD, Lee I, Dall J, Forsberg R (2020) Characteristics of ice rises and ice rumples in Dronning Maud Land and Enderby Land, Antarctica. *J. Glaciol.*, **66**(260), 1064–1078 (doi: 10.1017/jog.2020.77)
- Golledge NR, Levy RH, McKay RM and Naish TR (2017) East Antarctic ice sheet most vulnerable to Weddell Sea warming. *Geophys. Res. Lett.*, **44**(5), 2343–2351 (doi: 10.1002/2016GL072422)

- Golledge NR, Kowalewski DE, Naish TR, Levy RH, Fogwill CJ and Gasson EGW (2015) The multi-millennial Antarctic commitment to future sea-level rise. *Nature*, **526**(7573), 421–425 (doi: 10.1038/nature15706)
- Greenbaum JS and 10 others (2015) Ocean access to a cavity beneath Totten Glacier in East Antarctica. *Nat. Geosci.*, **8**(4), 294–298 (doi: 10.1038/ngeo2388)
- Groh A and Horwath M (2021) Antarctic Ice Mass Change Products from GRACE/GRACE-FO Using Tailored Sensitivity Kernels. *Remote Sensing*, **13**(9), 1736 (doi: 10.3390/rs13091736)
- Haran T, Bohlander J, Scambos T, Painter T and Fahnestock M (2014) MODIS Mosaic of Antarctica 2008–2009 (MOA2009) Image Map, Version 1. NASA National Snow and Ice Data Center Distributed Active Archive Center [data set] (doi: 10.5067/4ZL43A4619AF)
- Haran T, Bohlander J, Scambos T, Painter T and Fahnestock M (2005) MODIS Mosaic of Antarctica 2003–2004 (MOA2004) Image Map, Version 1. NASA National Snow and Ice Data Center Distributed Active Archive Center [data set] (doi: 10.5067/68TBT0CGJSOJ)
- Herraiz-Borreguero L, Allison I, Craven M, Nicholls KW and Rosenberg MA (2013) Ice shelf/ocean interactions under the Amery Ice Shelf: Seasonal variability and its effect on marine ice formation. *J. Geophys. Res. Oceans*, **118**, 7117–7131 (doi:10.1002/2013JC009158)
- Hersbach H, Bell B, Berrisford P, Biavati G, Horányi A, Muñoz Sabater J and 9 others (2023) ERA5 hourly data on single levels from 1940 to present. Copernicus Climate Change Service (C3S) Climate Data Store (CDS) (doi: [10.24381/cds.adbb2d47](https://doi.org/10.24381/cds.adbb2d47)) (Accessed on 16-11-2024)
- Hattermann T, Nost O, Lilly J and Smedsrud L (2012) Two years of oceanic observations below the Fimbulisen, Antarctica. *Geophys. Res. Lett.*, **39**, 12605 (doi: 10.1029/2012GL051012)
- Hill E, Carr R, Stokes CR and Gudmundsson HG (2018) Dynamic changes in outlet glaciers in northern Greenland from 1948 to 2015. *The Cryosphere*, **12**(10), 3243–3263 (doi: 10.5194/tc-12-3243-2018)
- Holt TO and Glasser NF (2022) Changes in area, flow speed and structure of southwest Antarctic Peninsula ice shelves in the 21st century. *J. Glaciol.*, **68**(271), 927–945 (doi: 10.1017/jog.2022.7)
- Holt TO, Glasser NF, Quincey DJ and Siegfried MR (2013) Speedup and fracturing of George VI Ice Shelf, Antarctic Peninsula. *The Cryosphere*, **7**(3), 797–816 (doi: 10.5194/tc-7-797-2013)
- Howat IM and 8 others (2012) Rift in Antarctic Glacier: A Unique Chance to Study Ice Shelf Retreat. *Eos*, **93**(8), 77–88 (doi: 10.1029/2012EO080001)
- Humbert A and Steinhage D (2011) The evolution of the western rift area of the Fimbulisen, Antarctica. *The Cryosphere*, **5**(4), 931–944 (doi: 10.5194/tc-5-931-2011)
- Khazendar A, Schodlok MP, Fenty I, Ligtenberg SRM, Rignot E and van den Broeke, MR (2013) Observed thinning of Totten Glacier is linked to coastal polynya variability. *Nat Commun*, **4**, 2857 (doi: 10.1038/ncomms3857)
- Khazendar A and Jenkins A (2003) A model of marine ice formation within Antarctic ice shelf rifts. *J. Geophys. Res.*, **108** (C7), 3235. 13, (doi: 10.1029/2002JC001673)
- Kim KT, Jezek KC and Sohn HG (2001) Ice shelf advance and retreat rates along the coast of Queen Maud Land, Antarctica. *J. Geophys. Res.: Oceans*, **106**(C4), 7097–7106 (doi: 10.1029/2000jc000317)

- Konrad H and 6 others (2018) Net retreat of Antarctic glacier grounding lines. *Nat. Geosci*, **11**, 258–262 (doi: 10.1038/s41561-018-0082-z)
- Kulesa B, Jansen D, Luckman A, King EC and Sammonds PR (2014) Marine ice regulates the future stability of a large Antarctic ice shelf. *Nat. Commun.*, **5** (3707) (doi: 10.1038/ncomms4707)
- Langley K and 8 others (2014) Low melt rates with seasonal variability at the base of Fimbulisen, East Antarctica, revealed by in situ interferometric radar measurements. *Geophys. Res. Lett.*, **41**(22), 8138–8146 (doi: 10.1002/2014GL061782)
- Larour E, Rignot E, Poinelli M and Scheuchl B (2021) Physical processes controlling the rifting of Larsen C Ice Shelf, Antarctica, prior to the calving of iceberg A68. *Proc Natl Acad Sci USA*, **111**(40) e2105080118 (doi: 10.1073/pnas.2105080118)
- Larour E, Rignot E, Joughin I and Aubry D (2005) Rheology of the Ronne Ice Shelf, Antarctica, inferred from satellite radar interferometry data using an inverse control method, *Geophys. Res. Lett.*, **32**(L05503) (doi:10.1029/2004GL021693)
- Larour E, Rignot E and Aubry D (2004) Modelling of rift propagation on Ronne Ice Shelf, Antarctica, and sensitivity to climate change, *Geophys. Res. Lett.*, **31**, L16404 (doi:10.1029/2004GL020077)
- Lauber J and 6 others (2023) Warming beneath an East Antarctic ice shelf due to increased subpolar westerlies and reduced sea ice. *Nat. Geosci.* **16**, 877–885 (doi: 10.1038/s41561-023-01273-5)
- Lea JM, Mair DWF and Rea, BR (2014) Instruments and Methods: Evaluation of existing and new methods of tracking glacier terminus change. *J. Glaciol.*, **60**(220), 323–332 (doi: 10.3189/2014JoG13J061)
- Lenaerts JTM, van Meijgaard E, van den Broeke MR, Ligtenberg SRM, Horwath M and Isaksson E (2013) Recent snowfall anomalies in Dronning Maud Land, East Antarctica, in a historical and future climate perspective, *Geophys. Res. Lett.*, **40**, 2684–2688 (doi:10.1002/grl.50559)
- Li X, Rignot E, Mouginot J and Scheuchl B (2016) Ice flow dynamics and mass loss of Totten Glacier, East Antarctica, from 1989 to 2015. *Geophys. Res. Lett.*, **43**(12), 6366–6373 (doi: 10.1002/2016GL069173)
- Lunde T (1963) On the firn temperatures and glacier flow in Dronning Maud Land. *Årbok. Norsk Polar Institute, Oslo*, 7-24.
- MacAyeal DR, Rignot E and Hulbe CL (1998) Ice-shelf dynamics near the front of the Filchner-Ronne Ice Shelf, Antarctica, revealed by SAR interferometry: Model/interferogram comparison. *J. Glaciol.*, **44**, 419–428
- Mae S and Naruse R (1978) Possible causes of ice sheet thinning in the Mizuho Plateau. *Nature*, **273**, 291–292 (doi: 10.1038/273291a0)
- Mas e Braga M and 12 others (2023) A thicker Antarctic ice stream during the mid-Pliocene warm period. *Commun Earth Environ*, **4**(321) (doi: 10.1038/s43247-023-00983-3)
- Massom RA, Scambos TA, Bennetts LG, Reid P, Squire VA and Stammerjohn SE (2018) Antarctic ice shelf disintegration triggered by sea ice loss and ocean swell. *Nature*, **558**, 383–389 (doi: 10.1038/s41586-018-0212-1)
- Matsuoka K, and 19 others (2015) Antarctic ice rises and rumples: Their properties and significance for ice-sheet dynamics and evolution. *Earth-Science Reviews*, **150**, 724-745 (doi: 10.1016/j.earscirev.2015.09.004)

- McGranahan G, Balk D and Anderson B (2007) The rising tide: assessing the risks of climate change and human settlements in low elevation coastal zones. *IIED*, **19**(1), 17–37 (doi: 10.1177/0956247807076960)
- McGrath D, Steffen K, Scambos T, Rajaram H, Casassa G and Rodriguez Lagos JL (2012) Basal crevasses and associated surface crevassing on the Larsen C ice shelf, Antarctica, and their role in ice-shelf instability. *Annals of Glaciology*. **53**(60):10-18 (doi:10.3189/2012AoG60A005)
- Medley B and 6 others (2018) Temperature and Snowfall in Western Queen Maud Land Increasing Faster Than Climate Model Projections. *Geophys. Res. Lett.*, **45**(3), 1472–1480 (doi: 10.1002/2017GL075992)
- Melvold K and Rolstad CE (2000) Subglacial topography of Jutulstraumen outlet glacier, East Antarctica, mapped from ground-penetrating radar, optical and interferometric synthetic aperture radar satellite data. *Norsk Geografisk Tidsskrift*, **54**(4), 169-181 (doi: 10.1080/002919500448549)
- Melvold K, Hagen JO, Pinglot JF and Gundestrup N (1998) Large spatial variation in accumulation rate in Jutulstraumen ice stream, Dronning Maud Land, Antarctica. *Ann. Glaciol.*, **27**, 231–238 (doi: 10.3189/1998AoG27-1-231-238)
- Meredith M and 12 others (2019): Polar Regions. In: IPCC Special Report on the Ocean and Cryosphere in a Changing Climate [Pörtner HO, Roberts DC, Masson-Delmotte V, Zhai P, Tignor M, Poloczanska E, Mintenbeck K, Alegría A, Nicolai M, Okem A, Petzold J, Rama B, Weyer NM (eds.)]. Cambridge University Press, Cambridge, UK and New York, NY, USA, pp. 203–320 (doi: 10.1017/9781009157964.005)
- Miles BWJ, Stokes CR, Jenkins A, Jordan JR, Jamieson SSR and Gudmundsson GH (2023) Slowdown of Shirase Glacier, East Antarctica, caused by strengthening alongshore winds. *The Cryosphere*, **17**(1), 445–456 (doi: 10.5194/tc-17-445-2023)
- Miles BWJ, Jordan JR, Stokes CR, Jamieson SSR, Gudmundsson GH and Jenkins A (2021) Recent acceleration of Denman Glacier (1972–2017), East Antarctica, driven by grounding line retreat and changes in ice tongue configuration, *The Cryosphere*, **15**, 663–676 (doi: 10.5194/tc-15-663-2021)
- Miles BWJ, Stokes CR and Jamieson SSR (2018) Velocity increases at Cook Glacier, East Antarctica, linked to ice shelf loss and a subglacial flood event. *The Cryosphere*, **12**(10), 3123–3136 (doi: 10.5194/tc-12-3123-2018)
- Miles BWJ, Stokes CR and Jamieson SSR (2016) Pan-ice-sheet glacier terminus change in East Antarctica reveals sensitivity of Wilkes Land to sea-ice changes. *Sci. Adv.*, **2**(5) (doi: 10.1126/sciadv.1501350)
- Miles BWJ, Stokes CR, Vieli, A and Cox NJ (2013) Rapid, climate-driven changes in outlet glaciers on the Pacific coast of East Antarctica. *Nature*, **500**(7464), 563–566 (doi: 10.1038/nature12382)
- Mohajerani Y, Jeong S, Scheuchl B, Velicogna I, Rignot E and Milillo P (2021) Automatic delineation of glacier grounding lines in differential interferometric synthetic-aperture radar data using deep learning. *Scientific Reports*, **11**(1) (doi: 10.1038/s41598-021-84309-3)
- Moon T and Joughin I (2008) Changes in ice front position on Greenland's outlet glaciers from 1992 to 2007. *J. Geophys. Res.-Earth*, **113**(2) (doi: 10.1029/2007JF000927)

- Morlighem M- and 36 others (2020) Deep glacial troughs and stabilizing ridges unveiled beneath the margins of the Antarctic ice sheet. *Nat. Geosci.* **13**, 132–137 (doi: 10.1038/s41561-019-0510-8)
- Naruse R (1979) Thinning of the Ice Sheet in Mizuho Plateau, East Antarctica, *J. Glaciol.*, **24**, 45–52 (doi: 10.3189/S0022143000014635)
- Nicholls KW, Abrahamsen EP, Heywood KJ, Stansfield K and Østerhus S (2008) High-latitude oceanography using autosub autonomous underwater vehicle, *Limnol. Oceanogr.*, **53**(5), 2309–2320 (doi:10.4319/lo.2008.53.5_part_2.2309)
- Nilsson J, Gardner AS and Paolo FS (2022) Elevation Change of the Antarctic Ice Sheet: 1985 to 2020. *Earth. Syst. Sci. Data*, **14**, 1-26 (doi: 10.5194/essd-2021-287)
- Nishio F, Mae S, Ohmae H, Takahashi S, Nakawo M and Kawada K (1989) Dynamical behaviour of the ice sheet in Mizuho Plateau, East Antarctica, Proc. NIPR Symp. *Polar Meteorol. Glaciol.*, **2**, 97–104
- Noble TL and 23 others (2020) The Sensitivity of the Antarctic Ice Sheet to a Changing Climate: Past, Present, and Future. *Rev. Geophys.*, **58**, e2019RG000663 (doi: 10.1029/2019RG000663)
- Nowicki S and 11 others (2013) Insights into spatial sensitivities of ice mass response to environmental change from the SeaRISE ice sheet modeling project I: Antarctica. *J. Geophys. Res.-Earth*, **118**(2), 1002–1024 (doi: 10.1002/jgrf.20081)
- Oppenheimer M and 14 others (2019) Sea Level Rise and Implications for Low-Lying Islands, Coasts and Communities. In Sea Level Rise and Implications for Low-Lying Islands, Coasts and Communities. In: IPCC Special Report on the Ocean and Cryosphere in a Changing Climate, 321–446 (doi: 10.1017/9755009157964.006)
- Payne AJ and 19 others (2021) Future Sea Level Change Under Coupled Model Intercomparison Project Phase 5 and Phase 6 Scenarios From the Greenland and Antarctic Ice Sheets. *Geophys. Res. Lett.*, **48**(16) (doi: 10.1029/2020GL091741)
- Picton HJ, Stokes CR, Jamieson SSR, Floricioiu D and Krieger L (2023) Extensive and anomalous grounding line retreat at Vanderford Glacier, Vincennes Bay, Wilkes Land, East Antarctica. *The Cryosphere*, **17**, 3593-3616 (doi: 10.5194/tc-17-3593-2023)
- Pritchard HD, Ligtenberg SRM, Fricker HA, Vaughan DG, van den Broeke MR and Padman L (2012) Antarctic ice-sheet loss driven by basal melting of ice shelves. *Nature*, **484**(7395), 502–505 (doi: 10.1038/nature10968)
- Rignot E and 7 others (2019) Four decades of Antarctic Ice Sheet mass balance from 1979-2017. *Environm. Sci.*, **116**(4), 1095–1103 (doi: 10.1594/PANGAEA.896940).y)
- Rignot E, Mouginot, J and Scheuchl B (2017) MEaSUREs Antarctic Boundaries for IPY 2007-2009 from Satellite Radar, Version 2. Boulder, Colorado USA. NASA National Snow and Ice Data Center Distributed Active Archive Center. (doi: 10.5067/AXE4121732AD)
- Rignot E, Mouginot J and Scheuchl B (2016) MEaSUREs Antarctic Grounding Line from Differential Satellite Radar Interferometry, Version 2. NASA National Snow and Ice Data Center Distributed Active Archive Center (doi: 10.5067/IKBWW4RYHF1Q)
- Rignot E, Jacobs S, Mouginot J and Scheuchl B (2013) Ice-shelf melting around antarctica. *Science*, **341**(6143), 266–270 (doi: 10.1126/science.1235798)

- Rignot E, Mouginot J and Scheuchl B (2011) Antarctic grounding line mapping from differential satellite radar interferometry. *Geophys. Res. Lett.*, **38**(10) (doi: 10.1029/2011GL047109)
- Rolstad C, Whillans IM, Hagen JO and Isaksson E (2000) Large-scale force budget of an outlet glacier: Jutulstraumen, Dronning Maud Land, East Antarctica. *Ann. Glaciol.*, **30**, 35–41 (doi: 10.3189/172756400755820642)
- Scambos TA, Haran TM, Fahnestock MA, Painter TH and Bohlander J (2007) MODIS-based Mosaic of Antarctica (MOA) data sets: Continent-wide surface morphology and snow grain size. *Remote Sens. Environ.*, **111**, 242–257 (doi: 10.1016/j.rse.2006.12.020)
- Schlosser E, Manning KW, Powers JG, Duda MG, Birnbaum G and Fujita K (2010) Characteristics of high-precipitation events in Dronning Maud Lan. Antarctica. *J. Geophys. Res.*, **115**, D14107 (doi:10.1029/2009JD013410)
- Schröder L, Horwath M, Dietrich R, Helm, V Van Den Broeke MR and Ligtenberg SRM (2019) Four decades of Antarctic surface elevation changes from multi-mission satellite altimetry. *The Cryosphere*, **13**(2), 427–449 (doi: 10.5194/tc-13-427-2019)
- Seroussi H and 11 others (2020) ISMIP6 Antarctica: A multi-model ensemble of the Antarctic ice sheet evolution over the 21st century. *The Cryosphere*, **14**(9), 3033–3070 (doi: 10.5194/tc-14-3033-2020)
- Shepherd A and 9 others (2019) Trends in Antarctic Ice Sheet elevation and mass. *Geophysical Research Letters*, **46**, 8174–8183. (doi: 10.1029/2019GL082182)
- Shepherd A and 19 others (2012) A reconciled estimate of ice-sheet mass balance. *Science*, **338**(6111), 1183–1189 (doi: 10.1126/science.1228102)
- Shepherd A, Wingham D, Wallis D, Giles K, Laxon S and Sundal AV (2010) Recent loss of floating ice and the consequent sea level contribution, *Geophys. Res. Lett.*, **37**(L13503) (doi:10.1029/2010GL042496)
- Smedsrud LH, Jenkins A, Holland DM and Nøst OA (2006) Modeling ocean processes below Fimbulisen, Antarctica, *J. Geophys. Res.*, **111**, C01007 (doi:10.1029/2005JC002915)
- Smith B and 13 others (2020) Pervasive ice sheet mass loss reflects competing ocean and atmosphere processes. *Science*, **368**(6496), 1239–1242 (doi: 10.1126/science.aaz5845)
- Stokes CR and 15 others (2022) Response of the East Antarctic Ice Sheet to past and future climate change. *Nature*, **608**(7922), 275–286 (doi: 10.1038/s41586-022-04946-0)
- Swithinbank C, McClain P and Little P (1977) Drift Tracks of Antarctic Icebergs. *Polar Record*, **18**(116), 495–501 (doi: 10.1017/S0032247400000991)
- The IMBIE Team (2023) Mass balance of the Greenland and Antarctic ice sheets from 1992 to 2020. *Earth Syst. Sci. Data*, **15**, 1597–1616 (doi: 10.5194/essd-15-1597-2023)
- Timmermann R, Wang Q, Hellmer HH (2012) Ice-shelf basal melting in a global finite-element sea-ice/ice-shelf/ocean model. *Annals of Glaciology*, **53**(60):303-314 (doi:10.3189/2012AoG60A156)
- Toh H and Shibuya K (1992) Thinning rate of ice sheet on Mizuho Plateau, East Antarctica, determined by GPS differential positioning. *Recent progress in Antarctic earth sciences*, 579–583
- van Autenboer T and Declair H (1969) Airborne Radio-glaciological investigation during the 1969 Belgian Antarctic expedition. *Bull. Soc. belge Géol., Paléont., Hydrol.*, **78**(2), 87-100
- Vinje TE (1975) Drift av Trolltunga i Weddellhavet. Årbok. Norsk Polar Institute, Oslo, 213–214

- Walker CC and Gardner AS (2019) Evolution of ice shelf rifts: Implications for formation mechanics and morphological controls. *ESPL*, **526**(2019) 115764 (doi: 10.1016/j.epsl.2019.115764)
- Walker CC, Bassis JN, Fricker HA and Czerwinski RJ (2015) Observations of interannual and spatial variability in rift propagation in the Amery Ice Shelf, Antarctica, 2002-14. *J. Glaciol.*, **61**(226), 243–252 (doi: 10.3189/2015JoG14J151)
- Walker CC, Bassis JN, Fricker HA and Czerwinski RJ (2013) Structural and environmental controls on Antarctic ice shelf rift propagation inferred from satellite monitoring. *J. Geophys. Res. Earth Surf.*, **118**, 2354–2364 (doi:10.1002/2013JF002742)
- Wolmarans LG and Kent LE (1982) Geological investigations in western Dronning Maud Land, Antarctica—a synthesis. *S. Afr. J. Antarct. Res.*, Supplement 2, 93
- Zwally HJ, Robbins JW, Luthcke SB, Loomis BD and Réy F (2021) Mass balance of the Antarctic ice sheet 1992-2016: Reconciling results from GRACE gravimetry with ICESat, ERS1/2 and Envisat altimetry. *J. Glaciol.*, **67**(263), 533–559. (doi: 10.1017/jog.2021.8)
- Zwally HJ, Giovinetto MB, Beckley MA and Saba JL (2012) Antarctic and Greenland Drainage Systems, GSFC Cryospheric Sciences Laboratory
- Zwally HJ and Giovinetto MB (2011) Overview and Assessment of Antarctic Ice-Sheet Mass Balance Estimates: 1992-2009. *Surv. Geophys.*, **32**(4–5), 351–376. (doi: 10.1007/s10712-011-9123-5)